



HAL
open science

Electron irradiation induced aging effects on radiative recombination properties of quadruple cation organic-inorganic perovskite layers

Pierfrancesco Aversa, Senol Öz, Eunhwan Jung, Olivier Plantevin, Olivier Cavani, Nadège Ollier, Jean-Eric Bourée, Bernard Geffroy, Tsutomu Miyasaka, Sanjay Mathur, et al.

► To cite this version:

Pierfrancesco Aversa, Senol Öz, Eunhwan Jung, Olivier Plantevin, Olivier Cavani, et al.. Electron irradiation induced aging effects on radiative recombination properties of quadruple cation organic-inorganic perovskite layers. *Emergent Materials*, In press, 3, pp.133-160. 10.1007/s42247-020-00096-z . cea-02561816

HAL Id: cea-02561816

<https://cea.hal.science/cea-02561816>

Submitted on 4 May 2020

HAL is a multi-disciplinary open access archive for the deposit and dissemination of scientific research documents, whether they are published or not. The documents may come from teaching and research institutions in France or abroad, or from public or private research centers.

L'archive ouverte pluridisciplinaire **HAL**, est destinée au dépôt et à la diffusion de documents scientifiques de niveau recherche, publiés ou non, émanant des établissements d'enseignement et de recherche français ou étrangers, des laboratoires publics ou privés.



Distributed under a Creative Commons Attribution 4.0 International License



Electron irradiation induced aging effects on radiative recombination properties of quadruple cation organic-inorganic perovskite layers

Pierfrancesco Aversa¹ · Senol Öz^{2,3} · Eunhwan Jung² · Olivier Plantevin⁴ · Olivier Cavani¹ · Nadège Ollier¹ · Jean-Eric Bourée⁵ · Bernard Geffroy^{5,6} · Tsutomu Miyasaka³ · Sanjay Mathur² · Catherine Corbel¹

Received: 9 December 2019 / Accepted: 30 March 2020
© The Author(s) 2020

Abstract

Understanding the role of defects in hybrid organic inorganic perovskites (HOIPs) is critically important to engineer the stability and performance of photovoltaic devices based on HOIPs. Recent reports on multi-cation compositions of general formula $(A^1, A^2, A^3, A^4)Pb(X^1, X^2, X^3)_3$, where the A sites can be occupied by a distribution of 2–4 metallic/organic cations and X sites with halide anions have shown stabilization effects against the well-known methyl ammonium lead triiodide ($CH_3NH_3PbI_3$), although the underlying mechanism is not fully elucidated. Herein, polycrystalline layers of $4APb(IBr)_3$ perovskite, where A is occupied by a combination of Cs^+ (cesium ion), GA^+ (guanidinium), MA^+ (methylammonium), and FA^+ (formamidinium) ions were synthesized. To gain insight on the role of intrinsic defects, electron irradiation was used for introducing point defects in a controlled way in the quadruple-cation HOIPs. Our results show that the engineered defects in perovskites strongly influenced the absorption, photoluminescence, and time-resolved photoluminescence of these materials, probably due to introduction of additional energy levels that modify electronic and light emitting properties of the material. Furthermore, the irradiation-induced defects were found to strongly affect the aging behavior of HOIPs and modify their radiative recombination properties.

Keywords Quadruple-cation hybrid perovskites · Defects · Electron irradiation · Photoluminescence · Aging effects

1 Introduction

Due to their unique optoelectronic properties (high absorption coefficient in the visible range, long charge carrier lifetime, high carrier mobility) and their simple processability through both solution and gas phase techniques, the hybrid organic inorganic halide perovskites (HOIPs) have witnessed a seminal growth in their photovoltaic efficiencies reaching the performance of standard semiconductors like silicon [1]. Although a large body of data has become available on perovskite-based photovoltaic devices mostly based on compositional variations (isoelectronic substitutions), the perovskite technology suffers from a number of stress factors, such as instability of HOIPs under illumination (both solar and UV), atmospheric conditions (moisture and oxygen), and interfacial reactions (ion migration), which deteriorate their device performance and efficiency. In this context, the role of native vacancy defects has been discussed as a possible cause for solar cell degradation, carrier lifetime reduction as well as for the hysteresis in the current-voltage curve under illumination. Defect-related trap states can act as nonradiative

✉ Sanjay Mathur
sanjay.mathur@uni-koeln.de

✉ Catherine Corbel
catherine.corbel@polytechnique.edu

¹ LSI, CEA/DRF/IRAMIS, Ecole Polytechnique, CNRS, Institut Polytechnique de Paris, 91128 Palaiseau, France

² Institute of Inorganic Chemistry, University of Cologne, Greinstrasse 6, 50939 Cologne, Germany

³ Graduate School of Engineering, Toin University of Yokohama, 1614 Kuroganecho, Aoba, Yokohama, Kanagawa 225-8503, Japan

⁴ Laboratoire de Physique des Solides, CNRS, Université Paris-Saclay, 91405 Orsay, France

⁵ LPICM, CNRS, Ecole Polytechnique, Institut Polytechnique de Paris, Route de Saclay, 91128 Palaiseau, France

⁶ CEA, CNRS, NIMBE, LICSEN, Université Paris-Saclay, 91191 Gif-sur-Yvette, France

recombination centers, limiting photovoltaic devices performances. A full understanding of the nature of the defect-induced electronic states, as well as of their role on device performance and degradation, is still under debate [2].

The multi-cation HOIPs with the general formula $(A^1, A^2, A^3, A^4)Pb(X^1, X^2, X^3)_3$, where the A sites can be occupied by a distribution of 2 to 4 metallic/organic cations and X sites with halide anions, have recently demonstrated higher structural and environmental stability than the parent compound methylammonium lead triiodide ($CH_3NH_3PbI_3$; $MAPbI_3$). The substitutional mixing on cation and anion sites allows to find the optimal stoichiometry enabling structural stability of the perovskite materials. This can improve perovskite stability at high temperatures under photovoltaic operational conditions and its sensitivity to moisture and humidity [3].

In this work, polycrystalline films of a quadruple cation perovskite, $(GACsMAFA)Pb(I, Br)_3$, were synthesized. It was shown in recent studies [4, 5] that this quadruple cation-based halide perovskite composition is successfully integrated in solar cell technologies yielding stable efficiencies (20%) under operational conditions. In order to understand the perovskite defect properties, and to verify the concept of defect tolerance and self-healing associated to HOIPs [2], electron irradiation was used to introduce defects in a controlled manner in the quadruple-cation HOIPs films. One-megaelectronvolt electron irradiation resistance [6, 7] has been reported for $MAPbI_3$ -based solar cells. Moreover, implantation and irradiation resistance to protons with energies ranging between 50 keV and 68 MeV in $MAPbI_3$ [6–8] and $(FAMA)Pb(I, Br)_3$ [6] perovskite-based solar cells, respectively, has also been demonstrated. Recently, the effect of photoluminescence properties of 30 keV He ion irradiated $MAPbI_3$ perovskite layers [9] has been reported. Particle irradiation can open new roads for defect engineering in HOIPs as well as it can help to understand in a more complete way perovskite fundamental properties.

To address the question whether, depending on its nature and concentration, the defect population in $(GACsMAFA)Pb(I, Br)_3$ layers plays any role in their stability and carrier recombination, this work for the first time uses electron irradiation to introduce intrinsic involving vacancies and interstitials defects. For this purpose, a set of quadruple layers of the chemical composition $(GACsMAFA)Pb(I, Br)_3$ were deposited on glass substrates and irradiated with 1 MeV electrons introduced from the glass side and with an increasing fluence. Electrons were delivered by a Pelletron accelerator from National Electrostatic Corporation (NEC) in the SIRIUS facility located in Laboratoire des Solides Irradiés (LSI), Ecole Polytechnique – Palaiseau. The choice of performing irradiation from the glass side was to simulate the same geometry as applied for the sunlight illumination of solar cells.

To examine whether electron irradiation results in any change of the bandgap and of conduction/valence band edges, absorption measurements were performed on the complete set of both reference and irradiated HOIP films. The carrier radiative recombination and excited carrier lifetimes upon irradiation were monitored using photoluminescence (PL) and time-resolved photoluminescence (TRPL) studies. With PL, the response of the $(GACsMAFA)Pb(I, Br)_3$ perovskite film under continuous laser illumination was also investigated for comparison with the so called light soaking effect already observed in $MAPbI_3$ [10, 11] and with reference to the photoresponse of other mixed halide perovskites [12].

Our experimental findings evidently show that intrinsic defects affect the radiative recombination properties in $(GACsMAFA)Pb(I, Br)_3$ perovskite films. This effect was systematically monitored at increasing aging time after irradiation. The correlation between the absorption and PL emission spectra after post-irradiation aging indicated that the radiative recombination involves electronic states located near the band edges rather than deep levels inside the bandgap.

2 Experimental methods

Fabrication procedure Five $GA_{0.015}Cs_{0.046}MA_{0.152}FA_{0.787}Pb(I_{0.815}Br_{0.185})_3$ ($(GACsMAFA)Pb(I, Br)_3$) perovskite films (set-18) were fabricated in a same preparation run on $12 \times 12 \times 1$ mm³ glass substrates in a nitrogen filled glovebox. In addition, one reference film (rf-17) was fabricated in another preparation run under the same conditions as the set-18. The substrates were treated with UV ozone for 15 min. The precursor solution was prepared by dissolving GAI (0.02 M), CsI (0.09 M), MABr (0.2 M), FAI (1.1 M), PbI_2 (1.2 M), and $PbBr_2$ (0.3 M) in anhydrous dimethylformamide (DMF): dimethyl-sulfoxide (DMSO) (4:1, v/v) mixed solvent. The stoichiometry for the solid composition (see above) is derived from the solution composition. The perovskite precursor solution was spin coated onto glass substrates via three step spin coating at 2000 rpm, 5000 rpm, and 6000 rpm for 10 s, 25 s, and 25 s, respectively, with toluene anti-solvent dripped 45 s after the start of the spin coating process. The perovskite layer was annealed at 100 °C for 1 h in a nitrogen filled glovebox. Before any treatment, the set-18 layers were stored in dark and under dry N_2 atmosphere for 1 week. The rf-17 layer was characterized in its pristine state immediately after preparation.

Controlled defect introduction via electron irradiation Four layers of the set-18 were individually irradiated from the glass substrate side with the 1-MeV electron beam delivered by the SIRIUS Pelletron accelerator (LSI-Polytechnique). Each layer was successively mounted on a Cu sample holder. Then, the sample holder was fixed in a specifically designed irradiation

chamber kept at room temperature (300 K) and filled with N₂ atmosphere. A thermocouple put on the sample holder was used to control that no heating was produced during each layer irradiation.

The electron beam size diameter on the holder is about 17 mm with an intensity that is rather homogeneous where the 12 × 12 mm² layer is mounted. The glass thickness being the same for each layer, this ensures that the dose deposition is rather homogeneous in the layers. Each irradiation is performed at the same beam intensity. During each irradiation, the beam intensity is continuously monitored and kept at this same constant value. Consequently, each layer is irradiated with the same electron flux. Before the irradiations, a calibration procedure is performed to relate the electron beam intensity monitored during irradiation to the electron flux received by the layer. The layers are irradiated at increasing fluences by increasing the irradiation time. The value for the lower fluence, f_l, is 9 × 10¹² e⁻/cm² in the f_l layer. The fluences f₀ in the reference rf-f₀ layer and f_n in the electron irradiated f_n layers are n times f_l with n = 0, 1, 2, 3, 4.

Layer optical characterization Absorption, PL and TRPL spectra were recorded for the reference and electron irradiated layers of the set-18 after different aging periods. In addition, the evolution of the PL spectra was recorded under continuous illumination. During the aging, the layers of the set-18 were kept in dark under flowing N₂ atmosphere. The aging A0d, A20d, A53d, and A110d durations correspond to 0, 20, 53, and 110 days of aging after the end of electron irradiation. Absorption, PL, and TRPL were performed after the A53d and A110d aging. For the A0d one, only absorption was recorded whereas, for the A20d one, only PL&TRPL were recorded. Only the PL evolution under continuous illumination was recorded for the rf-17 layer in its pristine state immediately after its preparation. The delay between absorption and PL&TRPL measurements was +3d for A53d and +1d for A110d.

Absorption Absorption spectra were recorded in air and at room temperature (300 K) with a double beam UV-VIS spectrophotometer (Jenway) with a wavelength resolution of 1 nm. The incident light penetrates through the perovskite face and illuminates a rectangular spot of ~5 × 1 mm². To span the 300–1000 nm range of illumination, the intensity recording versus wavelength lasts 5 min. The incident flux is weak. A second measurement on the same layer yields to same absorption spectra than recorded during the first measurement. The (GACsMAFA)Pb(IBr)₃ layer/glass absorbance is directly estimated from the logarithm of the ratio between the incident and transmitted light through the layer/glass structure. To this signal, to correctly estimate only the (GACsMAFA)Pb(IBr)₃ layer absorbance, the glass absorption signal is subtracted.

The wavelength dependence of the absorbance in the HOIPs layers, A(λ), is related to that of the transmittance by the relationship $A(\lambda) = \log_{10}(1/t(\lambda))$. Consequently, according to the Lambert-Beer law, the absorbance is the product of the absorption coefficient α(λ) per the pathlength of the light L: $A(\lambda) = \alpha(\lambda)L/2.303$. The transmittance, t, is related to the reflectance, r, and the absorptance, a, in the layers via: $t = 1 - r - a$. The values, A_{exp}(λ), measured with the spectrophotometer gives $A_{exp}(\lambda) = (1/t_{exp}(\lambda))$ where $1 = a(\lambda) + t_{exp}(\lambda)$. They are consequently equal to the A(λ) values only in the wavelength region where the scattered part of the incident light compared to the absorptance a(λ) is negligible ($r/a(\lambda) < 1$). In the following, it is considered that this is a valid assumption for the investigated (GACsMAFA)Pb(IBr)₃ HOIPs that have dull surface aspects as MAPbI₃ [13].

Luminescence For the pristine rf-17 layers and the layers set-18, the luminescence properties were first monitored by performing PL under continuous illumination. Then, for the five layers of the set-18, TRPL measurements were performed at the end of the continuous illumination after a dark period of 3 min.

For the rf-17 (GACsMAFA)Pb(IBr)₃ pristine layer, a 488 nm Coherent Sapphire laser was used at a 20 μW applied power to continuously illuminate a spot diameter of 1 μm in the central region of the layer. The layer was kept in air and at room temperature during illumination. The PL spectra at increasing illumination time were recorded with a wavelength resolution of 1 nm using an Andor spectrometer (Shamrock 303) connected to an Andor Si CCD camera (iDus Series).

For the set-18, both PL spectra under illumination and TRPL spectra were systematically recorded in the same environmental conditions as PL under illumination for rf-17, i.e., air and room temperature (~300 K). Measurements were performed in a reflection geometry at 45° using a Quantamaster 8000 spectrofluorometer equipped with a R13456 photomultiplier (Hamamatsu). To respectively conduct PL and TRPL, the spectrofluorometer was employed in two different acquisition modes: the “Steady State-Vis” mode for (steady state) PL and the “time-correlated single-photon counting (TCSPC)” one for TRPL. The PL spectra were recorded with a wavelength resolution of 1 nm during continuous illumination with a 454 nm Violet Blue Laser Diode (Cnilaser). A bandpass filter centered at 454 nm was used to eliminate the laser spectral wings. The laser diode delivered an applied power of 20 mW to illuminate a spot of about 1.5 mm diameter in the layer center. For TRPL, the lifetime decay spectra were recorded using a pulsed nano-LED emitting at 482 nm. The LED emitted pulses with energy of 14 pJ/pulse, duration of about 100 ps with a repetition rate of 10 kHz. The laser spot has a diameter of about 250 μm diameter. The emission

signals were filtered through a high-pass filter centered at 488 nm before detection.

PL under illumination As regarding PL under illumination, the rf-17 pristine layer was optically excited through the perovskite face. For the set-18, the illumination was through the glass face. The reason is to investigate the regions of the perovskite layers through which sunlight in solar cells or electron beam in this work enters. In all cases, one unique spot located close to the layer center was investigated although the spot diameter was of $\sim 1 \mu\text{m}$ for rf-17 and of $\sim 1.5 \text{ mm}$ for the set-18. The exact position of the spot may vary from one aging to the other one for the set-18. Consequently, one considers in the following that the spots illuminated after the A0d, A53d, and A110d aging correspond to regions near the layer centers that are different.

For the rf-17 (GACsMAFA)Pb(I_{Br})₃ pristine layer, every min, the PL spectra were recorded under the 488 nm illumination during 300 min. For the (GACsMAFA)Pb(I_{Br})₃ layers irradiated at the different fluences (set-18), after the A20d, A53d, and A110d aging, the PL peak for each fluence (except f3 for aging 53d) was first measured after the first 3 min of 454 nm illumination and, then, every 5 min, during two successive cycles of continuous laser illumination. Each cycle lasts 15 min. The laser spot remains at the same position from the first to the second one. The two cycles are separated by a three mins period without illumination. The dark period is chosen of 3 min because this is the time necessary to change the spectrofluorometer configuration from the “Steady State-Vis” to TCSPC mode at the end of the second cycle of illumination. This procedure allows to estimate whether, during the configuration change, the PL spectrum for which the TRPL is recorded can be expected to significantly differ from the last one recorded under illumination.

TRPL after illumination After the two cycles of continuous illumination for the A20d, A53d, and A110d and for each fluence (except f3 for A53d), the TRPL decays were recorded for a window range centered on the PL peak wavelength which corresponds to the first one of the second illumination cycle. At least two different spots (diameter 250 μm) were investigated for each layer of the set-18 to examine whether the PL decay lifetime spectra are homogeneous over the layer region where the PL under illumination was recorded. The TRPL measurements last from 5 to 7 min depending on the layer state. Consequently, before the TRPL measurement, the first spot remains under dark about 3 min to change the spectrometer configuration. The second ones remain a longer time under dark, for about 8 to 10 min, depending on the recording time for the first one.

The decay lifetime spectra are recorded over a time window that is chosen to ensure that the background level is reached for each spectrum. The time resolution per channel

is 56 ns. The resolution function is within a channel. For each spot P_n, the Horiba fitting program “One-to-Four Exponentials” is used to fit the experimental decay spectra to the convolution of the sum of i ($1 \leq i \leq 4$) exponential decay components with the spectrometer resolution function and resolve the lifetime decay value τ_{iP_n} and their respective coefficients α_{iP_n} : $D(t) = \sum_{i=1}^2 \alpha_{iP_n} \exp\left(-\frac{t}{\tau_{iP_n}}\right)$, $\sum_i \alpha_{iP_n} = 1$. The average lifetime value is calculated from the fitting as: $\tau_{P_n} = \sum_i I_{iP_n} \tau_{iP_n}$ with the intensity $I_{iP_n} = \frac{\alpha_{iP_n} \tau_{iP_n}}{\sum_j \alpha_{jP_n} \tau_{jP_n}}$, $i = 1, 2$ and $\sum_i I_{iP_n} = 1$. The lifetime data associated to each layer hereafter are the values τ_{P_n} , τ_{iP_n} averaged over two stops per layer as follows: $\langle \tau_{P_n} \rangle_{P_n} = \frac{\sum_{n=1}^2 \tau_{P_n}}{2}$, $\langle \tau_1 \rangle_{P_n} = \frac{\sum_{n=1}^2 \tau_{1P_n}}{2}$, $\langle \tau_2 \rangle_{P_n} = \frac{\sum_{n=1}^2 \tau_{2P_n}}{2}$ and their corresponding intensity values. The standard deviations for these quantities are calculated and shown as error bars in the corresponding figures.

As a summary, Table 1 recalls the link between the layer names and states for which the optical characterizations are conducted.

3 Results

For the layers set-18, the absorption data are recorded over a much larger spot than those for which PL under illumination and TRPL are recorded. Furthermore, the A0d, A53d, and A110d spots for absorption were all selected at the center of the perovskite layers. The different PL and TRPL spots were also selected in the layer central region. In the following, it is considered that the absorption evolution as a function of aging duration results from the aging (N₂, dark). For the 1st PL recorded under illumination, there is the coupling of the aging (N₂, dark) with the 454 nm illumination lasting 3 min in air. For the TRPL, there is the coupling of aging (N₂, dark) with the cycles of 454 nm illumination in air–light (15 min); dark (3 min); light (15 min)-dark (3 min).

Aging after e-irradiation: energy dependence of absorbance

This paragraph concerns the fluence-induced aging of the energy dependence of the absorbance in the (GACsMAFA)Pb(I_{Br})₃ layers (set-18). For the A_jd aging, the conditions are $j(d) = 0/53/110$ under N₂ atmosphere in dark at $\sim 300 \text{ K}$.

As seen in Fig. 1, independently of the fluence and aging, three energy regions can be discriminated in the variation of the (GACsMAFA)Pb(I_{Br})₃ reference rf-f0 and the 1 MeV e-irradiated fn layers (at fn fluence) absorbances. The mean rate of the absorbance variation per eV, $\langle dA/dE \rangle$, is weak in the higher and lower energy range, i.e., for $E(\text{eV}) > 1.68$ and for $E(\text{eV}) < 1.6$, respectively. In contrast, it is quite strong for the steep step in the energy range $1.68 < E(\text{eV}) < 1.6$.

Table 1 Name, treatment, and characterization of the GAO.015Cs0.046MA0.15 2FA0.787Pb(I0.815Br0.185)3 layers spin coated on glass. The numbers 17 and 18 in the rf-17 and set-18 names refer to the year of the preparation date of the layers

Layer treatment	Pristine: as-prepared				
Layer name	rf-17				
Photoluminescence (PL)	PLj(488 nm, ϕ 1 μ m, 2548 W/cm ²); on (air, 300 K, 5 h); j = 1–300				
Layer treatment	Set-18 N ₂ atmosphere, dark, 300 K 7d aged, e-irradiated at fluence fn, Ajd aged				
Layer name	rf-f0	f1	f2	f3	f4
e-Fluence (f1)	0	1	2	3	4
Absorption (Abs)	Absorption air 300 K				
Photoluminescence (PL)	PLj (454 nm, ϕ 1.5 mm, 11 W/cm ²) (air, 300 K) on(15 min); off(3 min); on(15 min); j = 1–6				
Time-resolved PL (TRPL)	TRPL (482 nm, ϕ 250 μ m, 14 pJ/pulse, 100 ps, 10 kHz) (air, 300 K)				
Aging Ajd_Abs	A0d; A53d; A110d_Abs				
Aging Ajd_PL_TRPL	A20d; A53d; A110d_PL_TRPL				

In the higher energy range, $E(\text{eV}) > 1.68$, independently of fluence, the absorbance tends to increase with increasing energy. Aging induces a strong decrease in the absorbance values. For A0d (Fig. 1a), the absorbance values reach saturation (> 4.95) at the following $E(\text{eV})$ values: ~ 2.23 (rf-f0, f2, f4); ~ 2.28 (f3); ~ 2.33 (f1). For A53d (Fig. 1b) and A110d (Fig. 1c), the maximum absorbance value at $E(\text{eV}) \sim 2.33$ eV is reached for the reference rf-f0 layer and the absorbance values are only 2.48 and 2.15, respectively. Furthermore, the fluence dependence in this higher energy region becomes more marked as the aging duration increases from A0d to A110d. This effect is stronger for the lower fluences. The absorbance for the rf-f0 reference layer and the irradiated f1 layer has energy dependences that are quasi-superimposed up to 2.16 eV for A0d. They become fully separated for A53d, A110d. For the f2 to f4 fluences, the energy dependences for absorbance are still quasi-overlapped for the A53d aging. They start to slightly differ for the A110d aging.

In the lower energy range $E(\text{eV}) < 1.60$, the absorbance tends to decrease as energy decreases from 1.64 to 1.24 eV for A0/53/110d. Independently on the aging duration, the

absorbance values remain quite low, ~ 0.1 – 0.3 and present oscillations with higher amplitudes for the four fluences than for the rf-f0 reference layer.

The cutoff energy between the steep step ($1.68 < E(\text{eV}) < 1.60$) and the lower energy region ($E < 1.6$ eV) of the absorption spectra, as described in [14–18] and illustrated in Fig. 2, for the rf-f0 reference layer and the irradiated f2, f4 layers is used to estimate the optical bandgaps. Table 2 shows that, for the longer aging duration, A110d, the optical bandgap has a slight tendency to shrink by 0.02–0.03(2) eV with increasing fluence in the range $f2 \leq fn \leq f4$.

One remark is that the fluence-induced features in the absorbance energy dependence are easier to analyze after the normalization of the absorbances to their value at 1.8 eV (Fig. 1, inserts). For each aging duration, the normalized absorbance (Fig. 1, inserts) for each fluence overlap between 1.8 and 1.68 eV. The values in this range are super-imposed in lg scale on a straight line with a low slope. The steep step exhibits also a linear dependence in lg scale. As aging duration increases, clearly, three features appear: (i) the step shifts to lower energy; (ii) the fluence effect on the slope becomes

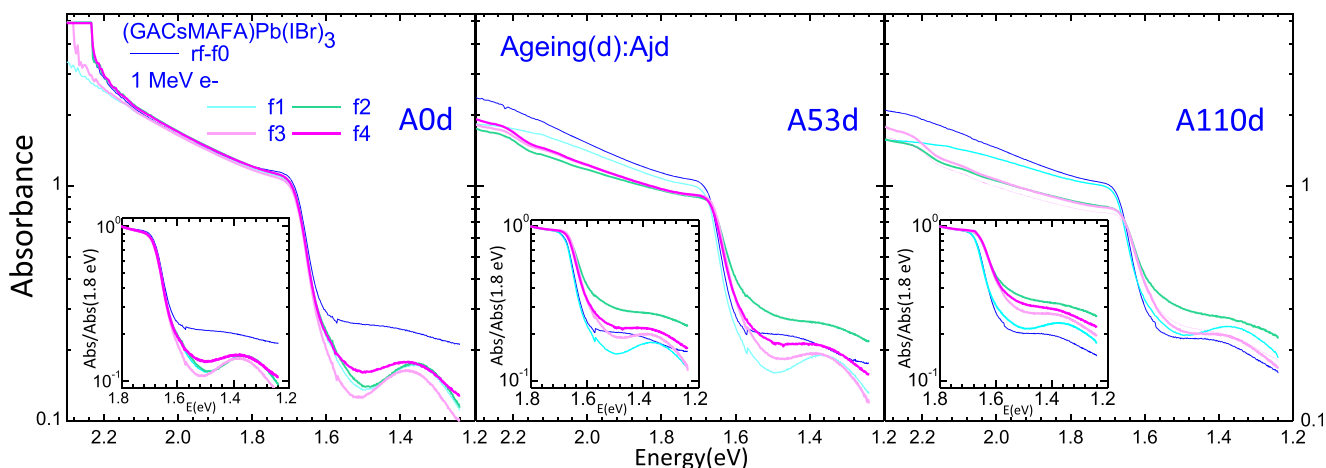


Fig. 1 Energy dependence of Absorbance (air, ~ 300 K) after aging in (GACsMAFA)Pb(IBr)₃ HOIPs for the reference Ajd_rf-f0 layer and the 1 MeV e-irradiated Ajd_fn layers at the fn fluence. The conditions for the

Ajd aging are $j(d) = 0/53/110$ under N₂ atmosphere in dark at ~ 300 K. Inserts: energy dependence of absorbance (air, ~ 300 K) after normalization to the value at 1.8 eV

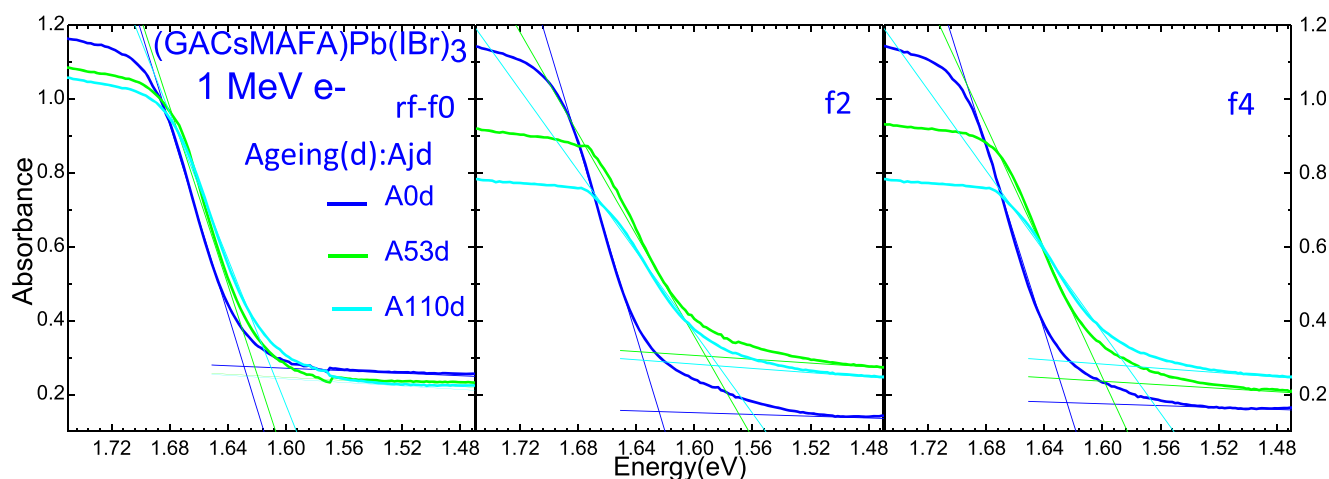


Fig. 2 Bandgap determination from the energy dependence of absorbance (air, ~ 300 K) after aging in (GACsMAFA)Pb(IBr)₃ HOIPs for the reference A_{jd}_rf-f0 layer and the 1 MeV e-irradiated A_{jd}_fn layers

at the f2 and f4 fluence. The conditions for the A_{jd} aging are $j(d) = 0/53/110$ under N₂ atmosphere in dark at ~ 300 K. The straight lines are used for the determination of the bandgap values in Table 2

stronger; and (iii) the step height decreases more strongly for the higher fluences, f2, f3, f4 than for the lower ones, rf_f0 (reference rf-f0 layer) and f1. The consequence of (iii) is that the fluence-dependence of the step height evolves with increasing aging duration from 0d(A0d) to 110d(A110d). Finally, in the lower energy range below the absorption edge, $1.2 \leq E(\text{eV}) \leq 1.60$, a same feature is also that, independently on aging, irradiation induces stronger absorbance oscillations with a base line that in lg scale, as for the rf-f0 reference layer, tend to decrease quasi-linearly with decreasing energy.

Aging after e-irradiation: fluence effect at each aging on PL

This paragraph concerns the 1st PL peak recorded in the set-18 of reference rf-f0 and the 1 MeV e-irradiated fn layers (at fn fluence) after 3 min of 454 nm continuous illumination at the end of each aging, A_{jd}, with $j = 20/53/110$. Figure 3 shows that, at each aging period, the 1 MeV electron irradiation induces a fluence dependence for the peak energy, the peak full width at half maximum (FWHM), and intensity ratio to the PL peak intensity of the reference rf-f0 layer in its A20d_rf-f0 state.

First PL peak energy: fluence effect for each aging after e-irradiation As seen in Fig. 3a, one easily notices that the PL peak energy at each aging has a fluence-induced distribution. The variation ranges at each aging have value in eV, A_{jd}-dEp_max-min(1st): 0.020(4)(A20d), 0.012(4)(A53d), 0.016(4) (A110d). As aging duration after electron irradiation increases from A0d to A110d, this range goes through a clear minimum at A53d.

For A20d, the PL peak energy goes through a maximum at the f1 fluence. For increasing fluence, the values in eV (Table 3) are respectively for A20d_fn-Ep(1st): 1.585(2)(rf-f0), 1.588(2)(f1), 1.584(2)(f2), 1.582(2)(f3), and 1.568(2)(f4). With respect to A20d_rf-f0-Ep(1st), the values of the peak shifts in eV are respectively for A20d_fn-dEp(1st): 0(rf-f0), 0.003(4) (f1), $-0.001(4)$ (f2), $-0.003(4)$ (f3), and $-0.0017(4)$ (f4). The blue-shift (f1) and the redshift (f2, f3) are at the limit of detection. There is however a clear tendency for irradiation to induce a redshift increase with increasing fluence from f2 to f4.

For A53d, the PL peak energy goes through a minimum at the f2 fluence. The values in eV (Table 3) are respectively for A53d_fn-Ep(1st): 1.582(2)(rf-f0), 1.580(2)(f1), 1.570(2)(f2), and 1.574(2)(f4). With respect to A53d_rf-f0-Ep(1st), the values of the peak shifts in eV are respectively for A53d_fn-

Table 2 Bandgaps after aging in (GACsMAFA)Pb(IBr)₃ HOIPs for the reference A_{jd}-rf-f0 and the 1 MeV e-irradiated A_{jd}_fn layers at the fn fluence. The conditions for the A_{jd} aging are $j(d) = 0/53/110$ under N₂ atmosphere in dark at ~ 300 K

A _{jd} _fn-Eg (eV)	rf-f0	f1	f2	f3	f4	vsf0_f1	vsf0_f2	vsf0_f3	vsf0_f4
A0d	1.63(1)	1.63(1)	1.63(1)	1.62(1)	1.63(1)	-0.00(2)	-0.00(2)	-0.01(2)	-0.00(2)
A53d	1.62(1)	1.62(1)	1.59(1)	1.60(1)	1.60(1)	-0.00(2)	-0.02(2)	-0.02(2)	-0.02(2)
A110d	1.61(1)	1.61(1)	1.59(1)	1.58(1)	1.58(1)	-0.00(2)	-0.02(2)	-0.03(2)	-0.03(2)
vsA0d_A53d	-0.01(2)	-0.01(2)	-0.04(2)	-0.02(2)	-0.03(2)				
vsA0d_A110d	-0.02(2)	-0.02(2)	-0.04(2)	-0.04(2)	-0.05(2)				
vsA53d_A110d	-0.01(2)	-0.01(2)	-0.00(2)	-0.02(2)	-0.02(2)				

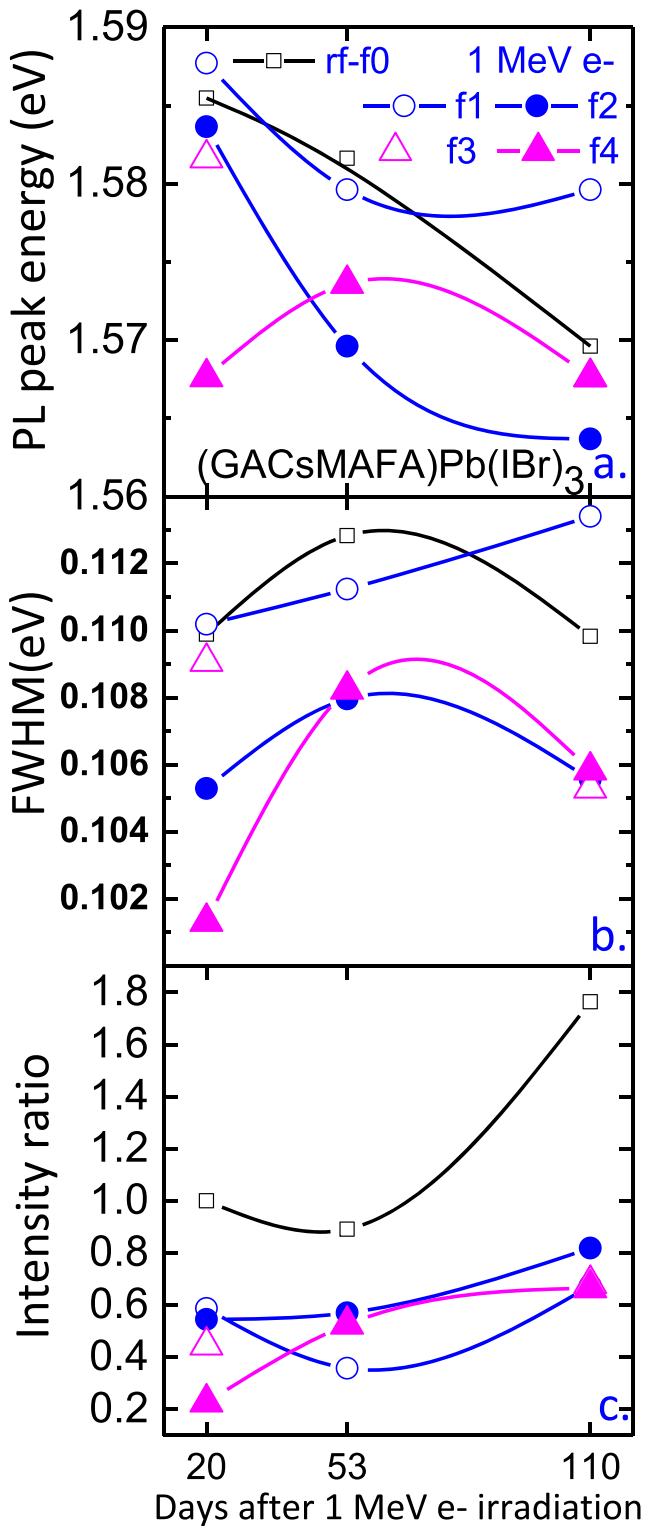


Fig. 3 Aging dependence of photoluminescence after 3-min illumination_ energy peak (a), FWHM (b), intensity ratio (c) in (GACsMAFA)Pb(IBr)₃ HOIPs for the reference A_jd_rf-f0 layer and the 1 MeV e-irradiated A_jd_fn layers at the fn fluence. The conditions for the A_jd aging are j(d)=20/53/110 under N₂ atmosphere in dark at ~300 K. Laser illumination is performed in (air, ~300 K) at the 454 nm wavelength and 11 W/cm² power density

dEp(1st): 0(rf-f0), -0.002(4)(f1), -0.012(4)(f2), and -0.008(4)(f4). Irradiation induces a redshift at any fluence in the range f1 ≤ fn ≤ f4. The redshift goes through a clear maximum at f2 fluence.

For A110d, the PL peak energy goes through a local maximum at f1 and a local minimum at f2. The values in eV are respectively for A110d_fn-Ep(1st): 1.570(2)(rf-f0), 1.580(2)(f1), 1.564(2)(f2), and 1.568(2) (f3,f4) (Table 4). With respect to A110d_Ep(rf-f0), values of the peak shifts in eV are respectively for A110d_fn-dEp(1st): 0(rf-f0), 0.010(4)(f1), -0.006(4)(f2), and -0.002(4)(f3,f4). For A110d, irradiation induces a marked blue shift for f1. Then, as fluence increases further to f4, there is a redshift that goes through a maximum at f2.

First PL peak FWHM: fluence effect for each aging after e-irradiation Figure 3 b shows that the FWHM at each aging has a fluence-induced distribution. The range of variation for the FWHM values goes through a minimum at A53d.

For A20d, the A20d_FWHMp_rf-f0/ fn values go through a local minimum at f1 fluence with increasing fluence. The FWHM values in eV are about 0.110(4)(rf-f0, f1), 0.105(4)(f2), 0.109(4)(f3), and 0.101(4)(f4). At most, they differ by -11 meV from the higher A20d_FWHMp(rf-f0) value.

For A53d, the A53d_FWHMp_rf-f0/ fn values decrease with increasing fluence. The FWHM values in eV are about 0.113(4)(rf-f0), 0.111(4)(f1), and 0.108(4)(f2, f4). They differ by at most -5 meV from the higher value A53d_FWHMp(rf-f0).

For A110d, the A110d_FWHMp_rf-f0/ fn values go through a maximum for f1. The FWHM values in eV are about 0.110(4)(rf-f0), 0.114(4)(f1), and 0.106(4)(f2, f3, f4). They differ by at most -8 meV from the higher A110d_FWHMp(f1) value.

First PL peak intensity: fluence effect for each aging after e-irradiation At each aging, irradiation induces a fluence dependence of the PL peak intensity, A_jd_Ip_fn. One notices in Fig. 3c that the values of the ratios to the PL peak intensity of A20d_rf-f0, A_jd_Ip_fn/A20d-Ip_rf-f0, vary in a range that goes through a weak minimum at A53d.

For A20d, the peak intensity ratio decreases with increasing fluence: 1 (rf-f0), 0.6 (f1, f2), 0.5(f3), 0.2 (f4). The relative variation to the A20d_rf-f0 peak intensity, A20d_fn-dIp(%), tends to increase with increasing fluence: from -40% (f1,f2) to -80% (f4).

For A53d, the PL peak intensity ratio goes through a minimum for f1 as fluence increases: 0.8(rf-f0), 0.4(f1), 0.6 (f2, f4). The relative variations to the A20d-rf-f0 peak intensity, A53d_fn-dIp(%), have associated values: -20% (rf-f0), -60% (f1), -40% (f2, f4). It follows that A53d aging induces a decrease of the peak intensity in the A53d_rf-f0 layer of about 20%. The decrease is reinforced by irradiation in the

Table 3 First Photoluminescence peaks after aging in (GACsMAFA)Pb(IBr)₃ HOIPs for the reference Ajd-rf-f0 and the 1 MeV e-irradiated Ajd_fn layers at the fn fluence. The conditions for the Ajd aging are j(d) = 0/53/110 under N₂ atmosphere in dark at ~300 K

Ajd_fn-Ep(eV)	rf-f0	f1	f2	f3	f4	vsf0_f1	vsf0_f2	vsf0_f3	vsf0_f4
A20d	1.585(2)	1.588(2)	1.584(2)	1.582(2)	1.568(2)	0.003(4)	-0.001(4)	-0.003(4)	-0.017(4)
A53d	1.582(2)	1.580(2)	1.570(2)	-	1.574(2)	-0.002(4)	-0.012(4)	-	-0.008(4)
A110d	1.570(2)	1.580(2)	1.564(2)	1.568(2)	1.568(2)	0.010(4)	-0.006(4)	-0.002(4)	-0.002(4)
vsA20d_A53d	-0.003(4)	-0.008(4)	-0.014(4)	-	0.006(4)				
vsA20d_A110d	-0.015(4)	-0.008(4)	-0.020(4)	-0.014(4)	0.000(4)				
vsA53d_A110d	-0.012(4)	0.000(4)	-0.006(4)	-	-0.006(4)				

A53d_fn layers more strongly at the lower fluence f1, 60%, than at the higher fluences $f2 \leq fn \leq f4$. The irradiation effect tends to saturate for the higher fluences $f2 \leq fn \leq f4$ with the variations remaining quasi-constant, ~40%.

For A110d, the PL peak intensity ratio has the higher value for rf-f0, ~1.8, and then goes through a local maximum for f2 as fluence increases. The values are about 1.8 (rf-f0), 0.7 (f1), 0.9 (f2), and 0.7 (f3, f4). Compared to A20d_Ip(rf-f0), the corresponding relative variations, A110d_fn-dIp(%), are about 80% (rf-f0), -30% (f1), -10% (f2), and -30% (f3,f4). Aging at A110d induces a strong increase in the peak intensity for rf-f0 of about 40%. The increase is so strongly damped by irradiation that it is totally compensated at any fluence, $f1 \leq fn \leq f4$. The compensating effect goes through a minimum for the f2 fluence.

Aging after e-irradiation: fluence-induced aging of PL This paragraph concerns the aging dependence at each fluence of the 1st PL spectra in each layer of the set-18, the reference Ajd_rf-f0 layer and the Ajd_fn irradiated ones at the fn fluences. The aging behavior of the 1st PL spectra in the set-18 layers couples aging in the storing conditions (N₂, dark, 300 K) and 3 min of 454 nm continuous illumination (air, 300 K) necessary for their recording. The aging behavior for the PL spectra for each fluence in the irradiated Ajd_fn layers can be compared to that of the Ajd_rf-f0 one to examine the synergy effects between irradiation and the Ajd aging-illumination coupling. Figure 3 shows that the synergy effects strongly depend on fluence.

Table 4 Urbach energies in the (GACsMAFA)Pb(IBr)₃ HOIPs after aging in the reference Ajd-rf-f0 and the 1 MeV e-irradiated Ajd_fn layers at the fn fluence. The conditions for the Ajd aging are j(d) = 0/53/110 under N₂ atmosphere in dark at ~300 K

Ajd_fn-Eu (meV)	rf-f0	f1	f2	f3	f4	vsf0_f1	vsf0_f2	vsf0_f3	vsf0_f4
A0d	52(2)	47(2)	47(2)	47(2)	50(2)	-5(4)	-5(4)	-5(4)	-2(4)
A53d	53(2)	50(2)	83(2)	61(2)	67(2)	-3(4)	30(4)	8(4)	14(4)
A110d	59(2)	63(2)	100(2)	87(2)	90(2)	4(4)	41(4)	28(4)	31(4)
vsA0d_A53d	1(4)	3(4)	36(4)	14(4)	17(4)				
vsA0d_A110d	7(4)	16(4)	53(4)	40(4)	40(4)				
vsA53d_A110d	6(4)	13(4)	17(4)	26(4)	23(4)				

First PL peak energy: fluence-induced aging after e-irradiation As seen in Fig. 3a, increasing aging duration induces a fluence dependence of the peak energy in the range ~1.564–1.588 eV. The evolutions have shapes that differ for fluences f0 (rf-f0 reference layer) and f4 from those for f1, f2 fluences, that are similar. Compared to A20d-Ip(fn), this results in peak shifts that evolve as aging duration increases by 33d (A53d-A20d) and 90d (A110-A20d).

For the rf-f0 reference layer, there is a continuous decrease of the peak energy with increasing aging duration. The redshift for the former 33d (A53d-A20d) and the latter 47d (A110d-A53d) aging have respective values in eV: -0.003(4) (33d_rf-f0), -0.012(4) (47d_rf-f0). The 47d aging induces a stronger effect than the 33d one and, consequently, accentuate the redshift.

With respect to the peak energy value for each fluence, A20d_Ep(fn), the (A53d-A20d)_dEp(fn) peak shifts have values in eV: -0.014(4)(33d_f2), -0.008(4)(33d_f1), -0.003(4) (33d_rf-f0), +0.006(4)(33d_f4). This shows that the former 33d aging induces redshifts for $0 \leq fn \leq f2$ with a maximum for f2. It induces a unique blue-shift for the f4 fluence.

The (A110d-A20d)_dEp(fn) peak-shifts in eV are -0.020(4)(f2), -0.015(rf-f0), -0.014(f3), -0.008(f1), 0(f4). It follows that aging during 90d from A20d to A110d induces redshifts for $0 \leq fn < f4$ and no shift for f4. The redshift reaches a maximum for the f2 fluence.

For the rf-f0 reference layer, the aging process is accelerated as aging duration increases from 33d to 47d. The average redshift per day increases by a factor 2.8 during the former 33d to

the latter 47d. For $f_1 \leq f_n \leq f_2$, the aging process tends to slow down during the 47d aging with the redshift per day decreasing by a factor of 0.3 (f_2) or 0 (f_1). For the f_4 fluence, the 33d and 47d aging have opposite effects with the result that the later 47d aging compensates the changes induced during the former 33d aging. The redshift rate per day is slower by a factor of 0.7 for the 47d aging than for the 33d one.

First PL peak FWHM: fluence-induced aging after e-irradiation

As seen in Fig. 3b, the aging-dependent values for the peak FWHM are in the same range for fluences f_0 (rf- f_0 reference layer), f_1 and in lower ones for fluences f_2 , f_3 , f_4 : ~ 0.101 – 0.108 (f_2 , f_4), ~ 0.106 – 0.110 (f_3), ~ 0.110 – 0.113 (rf- f_0 , f_1).

The aging evolution of the PL peak FWHM has a similar shape for the rf- f_0 reference layer and the f_2 , f_4 irradiated ones with a maximum at A53d. This maximum is clearly absent for the f_1 irradiated layer where the FWHM continuously increases with increasing aging duration. It follows that aging for rf- f_0 , f_2 , f_4 layers has opposite effects during the former 33d period (A53d-A20d) and the latter 47d period (A110d-A53d) on the FWHM behavior.

The A20d-FWHM_{rf- f_0 /f $_n$} values are lower for the f_4 layer than for the rf- f_0 , f_2 layers. The A110d-FWHM_{rf- f_0 /f $_n$} values are quasi the same with respect to the A20d-FWHM_{rf- f_0 /f $_n$} values for rf- f_0 , f_2 layers. This results in a steeper maximum for the f_4 layer than for the rf- f_0 , f_2 layers.

Compared to the reference rf- f_0 layer, irradiation has consequently effects on the peak FWHM aging that appears to be stronger for the layers f_1 , f_4 than for the f_2 layer.

First PL peak intensity: fluence-induced aging after e-irradiation

As seen in Fig. 3c, the evolution of the PL peak intensity ratio, $A_{jd_Ip_rf-f_0/f_n}/A_{20d_Ip_rf-f_0}$, has a similar shape for the rf- f_0 reference layer and irradiated f_1 layer with a minimum value at A53d. The behaviors for the irradiated f_2 and f_4 layers are respectively different from those. The peak ratio for the f_2 layer remains quasi-constant from A20d to A53d and then increases. There is a continuous increase for the f_4 layer that tends to saturate between A53d and A110d. These features show that there is a fluence threshold $f_1 < f_n < f_2$ above which the aging effects become clearly different in the irradiated layers from those in the reference rf- f_0 one. Furthermore, for any aging duration, the higher peak intensity ratios are for the rf- f_0 layer. The ratios $A_{jd_Ip_rf-f_0/f_n}/A_{20d_Ip_rf-f_0}$ are below 1 except for rf- f_0 at A110d. Consequently, the irradiation-aging induces a decrease of the PL peak intensities for any fluence $f_1 \leq f_n \leq f_4$. When compared to A20d_{Ip}(rf- f_0), the coupling between aging and irradiation has the stronger effect for A20d_{Ip}(f_4), approx. -80% , and the lower one for A110d_{Ip}(f_2) approx. -20% .

Illumination-time dependence of PL: pristine layer Figure 4 shows that 488-nm illumination at high intensity in air has a strong effect on the PL spectra in the pristine rf-17 layer. As illumination time increases from 1 to 300 min, the differences between the last 300th and 1st PL spectra for the peak (i) energy, (ii) FWHM and (iii) intensity are respectively in eV and %: rf-17(i)-dEp_{~300K}(300th-1st) $\sim -0.058(1)$; (ii)-FWHM_{~300K}(300th-1st) $\sim 0.100(1)$; (iii)-dIp_{~300K}(300th-1st) ~ -100 . The detailed examination below shows that the stronger variations are during the 1st hr. of illumination for (i) and (iii) (Fig. 4b, d) and during the last 5th hr for (ii) (Fig. 4c).

rf-17_PL peak energy under continuous illumination The decrease of the PL peak energy during illumination can be separated in four stages that roughly begin and end at the following time (min): (i) 1–8; (ii) 10–18; (iii) 20–60 for the 1st hour; (iv) 240–300 for the 5th hour.

The (i) 1–8 stage (i.e., between 1 and 8 min) is the steeper one where the peak energy decreases during the first 8 min of illumination from 1.6426(5) to 1.6047(5) eV with an average decrease rate of approx. less than $-4.74 \times 10^{-3} > \text{eV/min}$. During this stage, the redshift is the higher for the first 2 min of illumination with a decrease rate, $-1.804 \times 10^{-2} \text{ eV/min}$, about 3 times higher than the average one.

Then, there is the (ii) 10–18 stage, a transitory quasi-steady state where the PL peak energy levels off at 1.6058(1) eV.

During the (iii) 20–60 stage, the PL peak energy slowly decreases, less than $-1.44 \times 10^{-4} > \text{eV/min}$ and reaches 1.5921(5) eV.

The (iv) 240–300 stage corresponds to a quasi-steady state with fluctuations in the range 1.5875(5)–1.5818(5) eV that slowly tend to decrease the peak energy at a rate of less than $-3.81 \times 10^{-5} > \text{eV/min}$ from 1.5863(5) to 1.5852(5).

rf-17_PL peak FWHM under continuous illumination The rf-17_FWHM has a simple evolution (Fig. 4c). From the 1st to the last 5th hour, there is a continuous increase. During the 1st hour, the rf-17_FWHM slowly increases with an average rate of $< 3.17 \times 10^{-4} > \text{eV/min}$. Its values increase from 0.099(1) to 0.118(1) eV. During the 5th hour, the rf-17_FWHM increases from 0.161(1) to 0.199(1) (1st) with a faster rate of $< 6.33 \times 10^{-4} > \text{eV/min}$.

rf-17_PL peak intensity under continuous illumination The evolution of the peak intensity in Fig. 4d can be separated in four stages that roughly begin and end at the following time (min): (i) 1–8; (ii) 10–18; (iii) 20–60 for the 1st hour; (iv) 240–300 for the 5th hour. These stages correspond to successive slowing-downs of the rf-17_{Ip} decrease rate (%/min): (i) $< -9.00 >$; (ii) $< -1.25 >$; (iii) $< -2.56 \times 10^{-1} >$; (iv) $< -7.32 \times 10^{-3} >$. During the 1st stage (i), the decrease is the highest

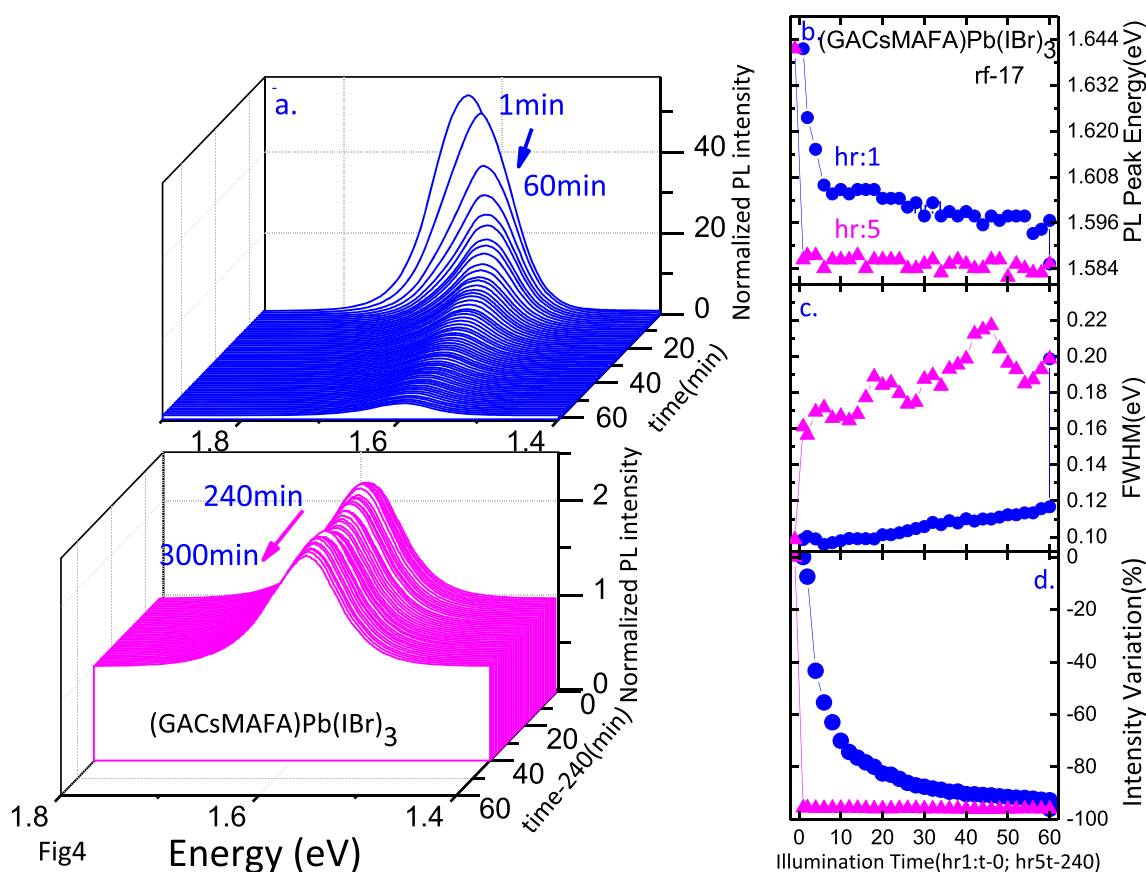


Fig. 4 Illumination-time dependence of photoluminescence intensity normalized to the background (a), energy peak (b), FWHM (c), intensity ratio (d) after aging in (GACsMAFA)Pb(I Br)₃ HOIPs for the

pristine rf-17. Laser illumination is performed in (air, ~300 K) at the 488 nm wavelength and 2548 W/cm² power density

during the first 2 and 4 min of illumination with a decrease rate of $-17.9\%/min$. The peak intensity decreases from 54.8 to 3.98% during the first hour and from 2.41 to 2.17% during the last hour.

Aging after electron irradiation: fluence effect on PL illumination-time dependence In the set-18 (reference Ajd_rf-f0 layer and the Ajd_fn irradiated ones at fn fluence), for each aging duration Ajd ($j(d) = 20, 53, 110$), the evolution of the PL spectra during the 454 nm illumination cycles depends on the electron irradiation fluence (Fig. 5). Furthermore, one notices that the evolution of the 4th-5th-6th spectra during the second cycle of 15-min illumination, is generally consistent with that of the 1st-2nd-3rd spectra during the first cycle of 15 min illumination. The dark period of 3 min between the two cycles of 15-min continuous illumination stops or induces a slight recovery of the PL evolution in most cases.

PL peak energy: fluence effect on the aging of its illumination-time dependence After each aging period, the peak energy in Fig. 5a–e has illumination time-dependence that varies with fluence. The decrease is generally steeper during the first illumination cycle. It tends to level off than

during the second one. The most striking effect of fluence on the peak energy of each n^{th} PL spectra recorded during illumination is that, at each aging, the fluence f_l plays a unique role. Independently on the aging period, this is the fluence at which each n^{th} PL peak energy goes through a maximum under illumination. These values, $Ajd_f_l - Ep(n^{\text{th}})$, in eV are higher for A20d than for A53d and, only slightly, for A53d than for A110d.

For A20d, the n^{th} PL spectra with $4 \leq n \leq 6$ spectra recorded during the second illumination cycle exhibit one peak. The n^{th} peak energy varies in a fluence-dependent range such that it increases with fluence as follows: $A20d_f4 - Ep(n^{\text{th}}) < f2 - Ep(n^{\text{th}}) < f3 - Ep(n^{\text{th}}) < rf-f0 - Ep(n^{\text{th}}) < f1 - Ep(n^{\text{th}})$. In respect to $A20d_rf-f0, fn - Ep(1st)$, the redshifts for the 6th spectra recorded at the end of the illumination cycles, $A20d_rf-f0, fn - dEp(6th)$ goes through a maximum for the f2 fluence where it reaches $-0.017(4)$ eV. The redshift is the smaller for the f1 fluence, at the limit of detection. These values are, in eV, $A20d_rf-f0, fn - dEp(6th)$: $-0.007(4)(rf-f0)$, $-0.004(4)(f1)$, $-0.017(4)(f2)$, $-0.014(4)(f3)$, $-0.010(4)(f4)$.

For A53d, the n^{th} PL spectra with $4 \leq n \leq 6$ spectra recorded during the second illumination cycle exhibit one peak. The n^{th} peak energy varies in a fluence-dependent range such that it

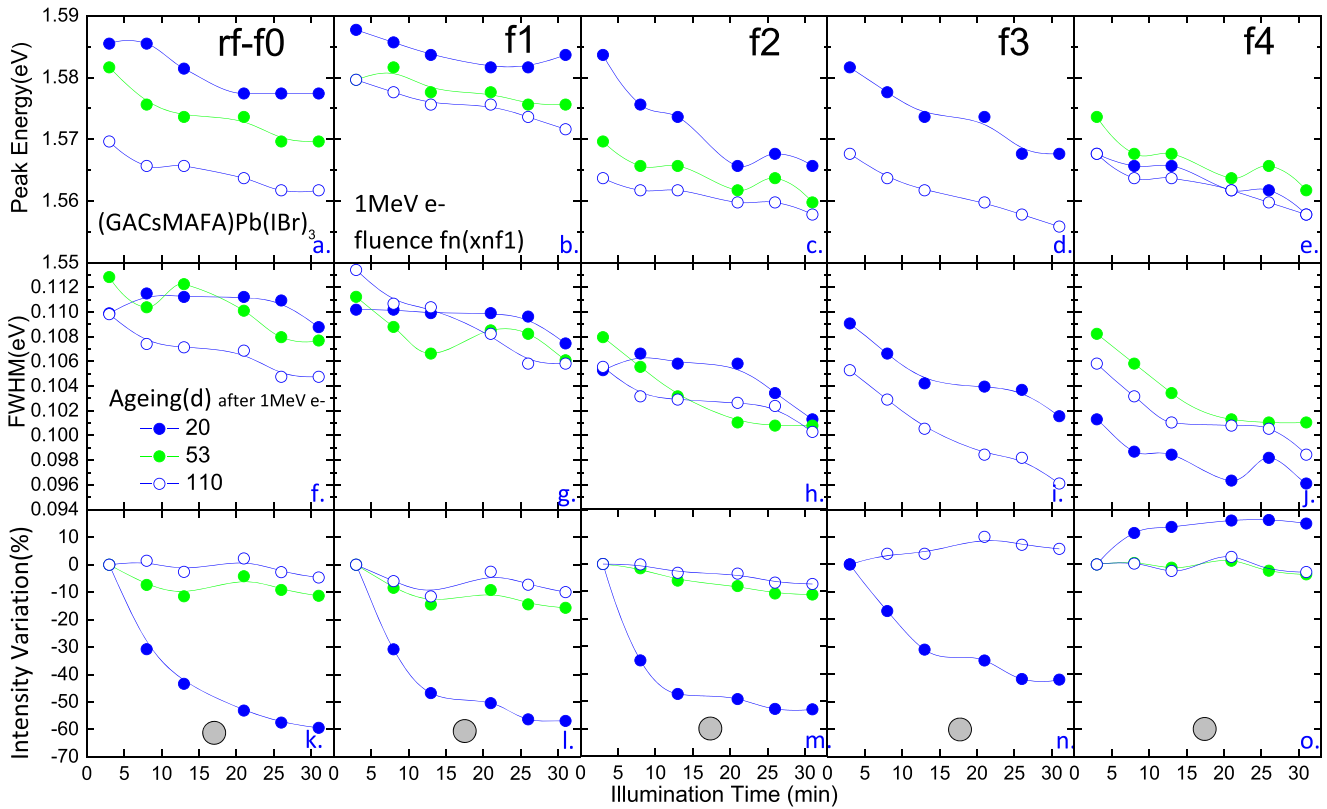


Fig. 5 Illumination-time dependence of photoluminescence energy peak (a–e), FWHM (f–l), intensity ratio (m–q) after aging in (GACsMAFA)Pb(I_{Br})₃ HOIPs for the A_{jd}_rf-f0 reference layer and the A_{jd}_fn 1 MeV e-irradiated layers at the fn fluence. The conditions for the A_{jd} aging are j(d) = 20/53/110 under N₂ atmosphere in dark at ~300 K.

Laser illumination is performed in (air, ~300 K) at the 454 nm wavelength and 11 W/cm² power density. Two cycles of 15 min of illumination are separated by a dark period of 3 min: light (15 min); dark (3 min); light (15 min)

increases with fluence as follows: A53d_f2-Ep(nth) <_f4-Ep(nth) <_rf-f0-Ep(nth) <_f1-Ep(nth). In respect to A53d_rf-f0/_fn-Ep(1st), the redshifts for the 6th spectra recorded at the end of the illumination cycles, A53d_rf-f0/_fn-dEp(6th), is maximum for the f0 (reference rf-f0 layer), f4 fluences where it reaches -0.012(4) eV. The redshift is the smaller for the f1 fluence. These values are, in eV, A53d_rf-f0/_fn-dEp(6th): -0.012(4)(rf-f0), -0.004(4)(f1), -0.010(4)(f2), -0.012(4)(f4).

For A110d, the nth PL spectra with 4 ≤ n ≤ 6 spectra recorded during the second illumination cycle exhibit one peak. The nth peak energy varies in a fluence-dependent range such that it increases with fluence as follows: A110d_f3-Ep(nth) <_f4-Ep(nth) ~_f2-Ep(nth) <_rf-f0-Ep(nth) <_f1-Ep(nth). With respect to A110d_rf-f0/_fn-Ep(1st), the redshifts for the 6th spectra recorded at the end of the illumination cycles, A110d_rf-f0/_fn-dEp(6th) goes through a maximum for the fluence f3 where it reaches -0.012(4) eV. They are quasi-equal for the fluences f0 (reference rf-f0 layer), f1, f2, f4, approx. -0.010(4) eV.

PL peak FWHM: fluence effect on the aging of its illumination-time dependence After each aging period, the PL peak FWHM

in Fig. 5f–j has illumination-time dependence that varies with fluence. The most striking effect of fluence on the peak FWHM is that, at any aging, the f2 fluence appears as a threshold value for which, for fn ≥ f2, there is a clear narrowing of the nth (1 ≤ n ≤ 4) spectra. The FWHM values for fn ≤ f1, A_{jd}_rf-f0/_fn-FWHM(nth), are ≥ 0.106 eV. The FWHM values for fn ≥ f2, A_{jd}_rf-f0/_fn-FWHM(nth), are ≤ 0.106 eV.

The FWHM values for each aging and fluence are always lower for the last spectra (6th) than for the first spectra recorded under illumination: A_{jd}_rf-f0/_fn-FWHM(6th) < A_{jd}_rf-f0/_fn-FWHM(1th). The spectra narrowing depends on aging and fluence.

For A20d, the FWHM values in eV for the 6th spectra decrease with increasing fluence: A20d_rf-f0-FWHM(6th): 0.108(4) ~_f1-FWHM(6th): 0.108(4) >_f2-FWHM(6th): 0.101(4) ~_f3-FWHM(6th): 0.101 >_f4-FWHM(6th): 0.096(4). For A53d, the narrowing become quasi-equal. A110d, the narrowing goes through a minimum for the f3 fluence. The lower value for A_{jd}_fn-FWHM(6th), 0.096(4) eV, is reached in two cases: A20d_f4-FWHM(6th); A110d_f3-FWHM(6th).

For each aging, the illumination-time dependence exhibits slight fluence dependent differences. The differences vary with the illumination cycle. The aging has different effects on the fluence dependence of each cycle. As concern the 1st to 3rd spectra recorded during the first illumination cycle, the main effect of aging is to increase the fluence range where the $A_{jd_rf-f0}/_{fn-FWHM}(n^{th})$ ($1 \leq n \leq 3$) values decrease with increasing illumination time. For A20d, a decrease of the $A_{20d_fn-FWHM}(n^{th})$ ($1 \leq n \leq 3$) values is observed only for $fn \geq f3$. For A53d, it already occurs for $fn \geq f1$. For A110d, it is already present in the rf-f0 reference layer. As concern the 4th to 6th spectra recorded during the second illumination cycle, the main aging effect is for the fluence f2. As aging increases from A20d to A110d, clearly the illumination dependence for $A_{jd_f2-FHWM}(n^{th})$ ($4 \leq n \leq 6$) is reduced: from decreasing for A20d to nearly flat for A53d, A110d.

PL peak intensity: fluence effect on the aging of its illumination-time dependence After each aging period, the PL peak intensity in Fig. 5k-o has illumination-time dependence that varies with fluence. For each aging, the shape changes suddenly with increasing fluence. The threshold fluence for these changes are A20d-f4, A53d-f3, and A110d-f4, respectively. The detailed analysis below shows that 1 MeV irradiation progressively affects the 454 nm illumination effect as fluence increases from f1 to f4. Increasing the fluence irradiation dampens the illumination effect more strongly for the shorter aging duration, A20d, than for the longer ones, A53d, A110d. The damping effect is the higher at the f4 fluence for A20d. It goes through a maximum at f3 for A110d.

For A20d, the illumination-time dependence is different for the lower fluence range, $fn \leq f3$, and the higher one, $f3 < fn \leq f4$. For $fn \leq f3$, the 454 illumination induces a steep decrease with increasing illumination time for the spectra ($1 \leq n \leq 3$) recorded during the first cycle. The decrease tends to level off during the second illumination cycle for the spectra ($4 \leq n \leq 6$). For the fluence f4, illumination with time induces an increase of the peak intensity that tends to level off during the first and second illumination cycles for the spectra $1 \leq n \leq 6$. Compared to the first peak ($n = 1$), the relative variation for the last peak, $A_{20d_fn-dI}(6th)$ progressively increase with increasing fluence: $-62\%(rf-f0) < -53\%(f1) < -50\%(f2) < -40\%(f3) < +13\%(f4)$.

For A53d, A110d, the illumination-time dependence has two type of shapes depending whether the fluence is in the lower range, $fn \leq f2$, or the higher one $f2 < fn \leq f4$. For $fn \leq f2$. The 454 nm illumination with time induces a small decrease in the peak intensity, $-20 \leq A_{20_dIp}(\%) \leq \sim 0$, during the first and second cycles for the spectra $1 \leq n \leq 6$. For the fluence range, $f2 < fn \leq f4$, the peak intensity tends to remain constant. For all layers (rf-f0 and fn irradiated ones), the dark period of 3 min seems to induce a small increase of the peak intensity

from the 4th to the 5th spectrum, $0 \leq A_{20_dIp-5th-4th}(\%) \leq \sim +5$, between the two cycles.

Aging after electron irradiation: fluence-induced aging dependence of PL decay The comparison of the experimental and fitted PL lifetime decay spectra versus increasing time in Fig. 6, $A_{jd_fn-TRPL}(t)$, for the fluences f1, f4 and j(d) = 20, 53, 110, illustrates that the increase of aging duration, from 20d(A20d) to 90d(A110d), tends to reduce the small difference between the time-dependence recorded over each spot per layer. This tendency is true for any fluence f0 (reference rf-f0 layer) $\leq fn \leq f4$, which suggests that the layers tend to become more homogeneous as aging duration increases. Figure 6 also illustrates that the decay slopes, $A_{jd_fn-TRPL}(t)$, vary differently with increasing aging. For A20/53d, the backgrounds $A_{jd_fn-TRPL-BKL}(t)$ are indeed higher for f4 than f1. For A110d, this is the opposite for the A110d $_{fn-TRPL-BKL}(t)$ that is lower for f4 than f1. This aging effect is reflected in the fluence -dependences of the spectra average lifetime, $A_{jd_<\tau_{Pn}>_{Pn_rf-f0}/_{fn}}$ and those of the two $A_{jd_fn_<\tau_i>_{Pn_rf-f0}/_{fn}}$, $A_{jd_fn_<I_i>_{Pn_rf-f0}/_{fn}}$ spectra components as seen in Fig. 7. The average lifetimes (Fig. 7a) go through a weak minimum, $A_{jd_<\tau_{Pn}>_{Pn_rf-f0}/_{fn} min$, that is located in different fluence ranges depending on aging and value in ns that increases with aging as follows: A20d $f2 \leq fn \leq f3$ -1440(10); A53d $_{f1}$ -1933(69); A110d $f2 \leq fn \leq f3$ -2410(50). The maximum values, $A_{jd_<\tau_{Pn}>_{Pn_rf-f0}/_{fn} max$ are reached at fluences that decrease with increasing aging and have values in ns that go through a minimum with increasing aging: A20d $f4$ -4435(600); A53d $_{rf-f0}$ -3004(466); A110d $_{rf-f0}$ -4275(300).

The lifetime components (Fig. 7b, c), $A_{jd_fn_<\tau_i>_{Pn_rf-f0}/_{fn}}$, with increasing fluence have shapes quite similar to those of $A_{jd_<\tau_{Pn}>_{Pn_rf-f0}/_{fn}}$. The minima, $A_{jd_fn_<\tau_i>_{Pn_rf-f0}/_{fn} min$, in ns are for the lower and higher component, respectively:

$$A_{jd_fn_<\tau_1>_{Pn_rf-f0}/_{fn} min \\ : A_{20d_f2 \leq fn \leq f3}; A_{53d_f1}; A_{110d_f2 \leq fn \leq f3}$$

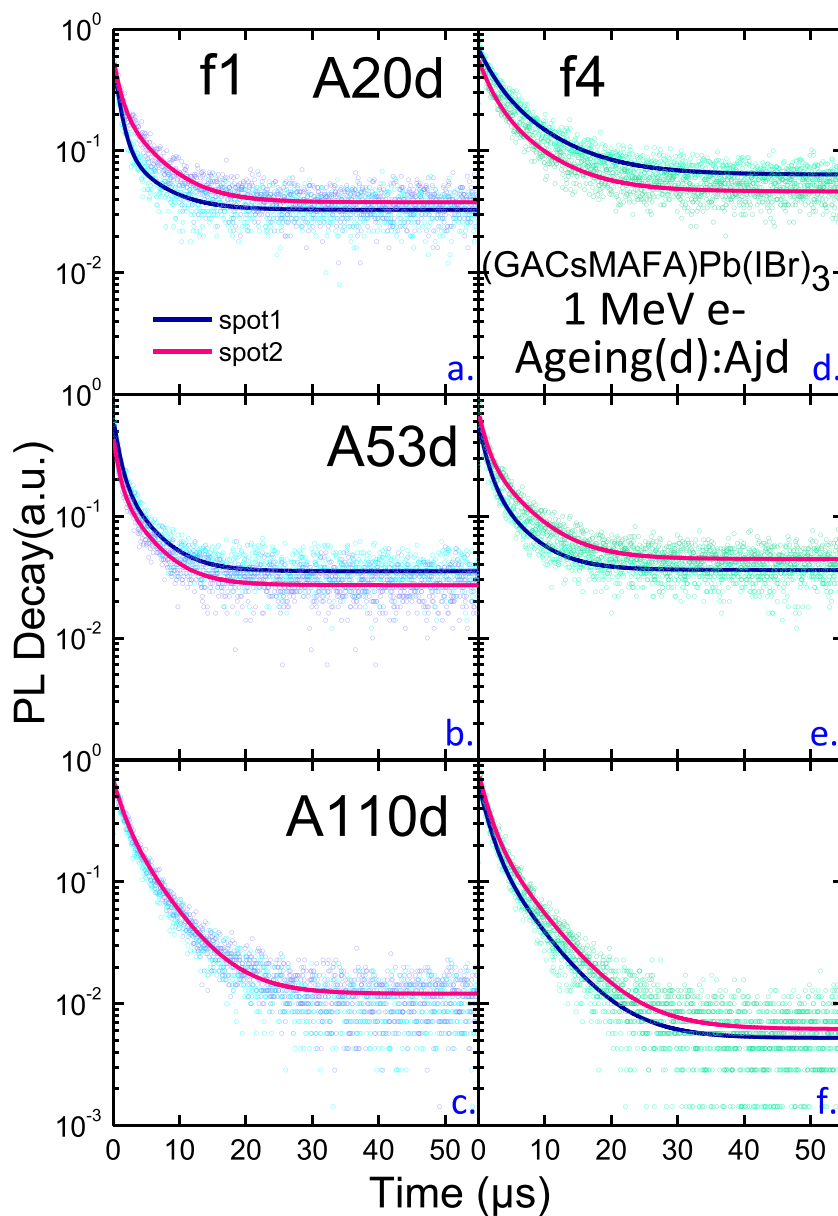
$$A_{jd_fn_<\tau_2>_{Pn_rf-f0}/_{fn} min \\ : A_{20d_f2 \leq fn \leq f3}; A_{53d_f1}; A_{110d_f2 \leq fn \leq f3}$$

The maxima $A_{jd_fn_<\tau_i>_{Pn_rf-f0}/_{fn} max$ are reached at fluences that decrease with increasing aging and have values in ns that go through a minimum with increasing aging:

$$A_{jd_fn_<\tau_1>_{Pn_rf-f0}/_{fn} max \\ : A_{20d_f4}; A_{53d_f0}; A_{110d_rf-f0}$$

$$A_{jd_fn_<\tau_2>_{Pn_rf-f0}/_{fn} max \\ : A_{20d_f4}; A_{53d_f0}; A_{110d_rf-f0}$$

Fig. 6 Time-resolved photoluminescence recorded after 30 min laser illumination (Fig. 5) over two Pn_Ajd spots after aging in (GACsMAFA)Pb(IBr)₃ HOIPs for the 1 MeV e-irradiated Ajd_fn layers at the f1 and f4 fluences. The conditions for the Ajd aging are j(d) = 20/53/110 under N₂ atmosphere in dark at ~300 K. The TRPL spectra are recorded using a nano-LED_482nm, 14 pJ/pulse energy, 100 ps pulse duration, and 10 kHz repetition rate. The laser spot has a diameter of about 250 μm diameter. Straight lines are fits to the experimental decays



The intensities for the lower component (Fig. 7d), $A_{jd} \langle I_1 \rangle_{Pn_rf-f0} /_{fn}$, with increasing fluence go through two local minima at f2, f4 for A20d and through a maximum at f2 for A53/110d. The values in % vary in the range $50 < A_{jd} \langle I_1 \rangle_{Pn_rf-f0} /_{fn} < 75\%$.

The contribution of each component, $A_{jd} \langle I_i \tau_i \rangle_{rf-f0} /_{fn}$ to the average lifetime vary with increasing fluence and aging. The stronger contribution (> 50%) is at any fluence and aging from the longer component. This reflects that the variation of the lifetime $A_{jd} \langle \tau_2 \rangle_{Pn_rf-f0} /_{fn}$, compensates the variation of its intensity $A_{jd} \langle I_2 \rangle_{Pn_rf-f0} /_{fn}$.

4 Discussion

As described above, 1 MeV electron irradiation at 300 K under N₂ atmosphere significantly affected the optical properties of the (GACsMAFA)Pb(IBr)₃ layers. The fluence dependence of quadruple HOIPs on the aging behavior (absorbance) and response to the illumination treatment was performed after each aging period (PL and TRPL) that showed the intrinsic defects created upon 1 MeV electron irradiation modified the electronic states that are optically active. Defects can have different types of interaction modes that apparently result in modified electronic states. The modes of interaction that appear predominant in the (GACsMAFA)Pb(IBr)₃ HOIP layers are discussed below to elucidate the beneficial effects of electronic irradiation.

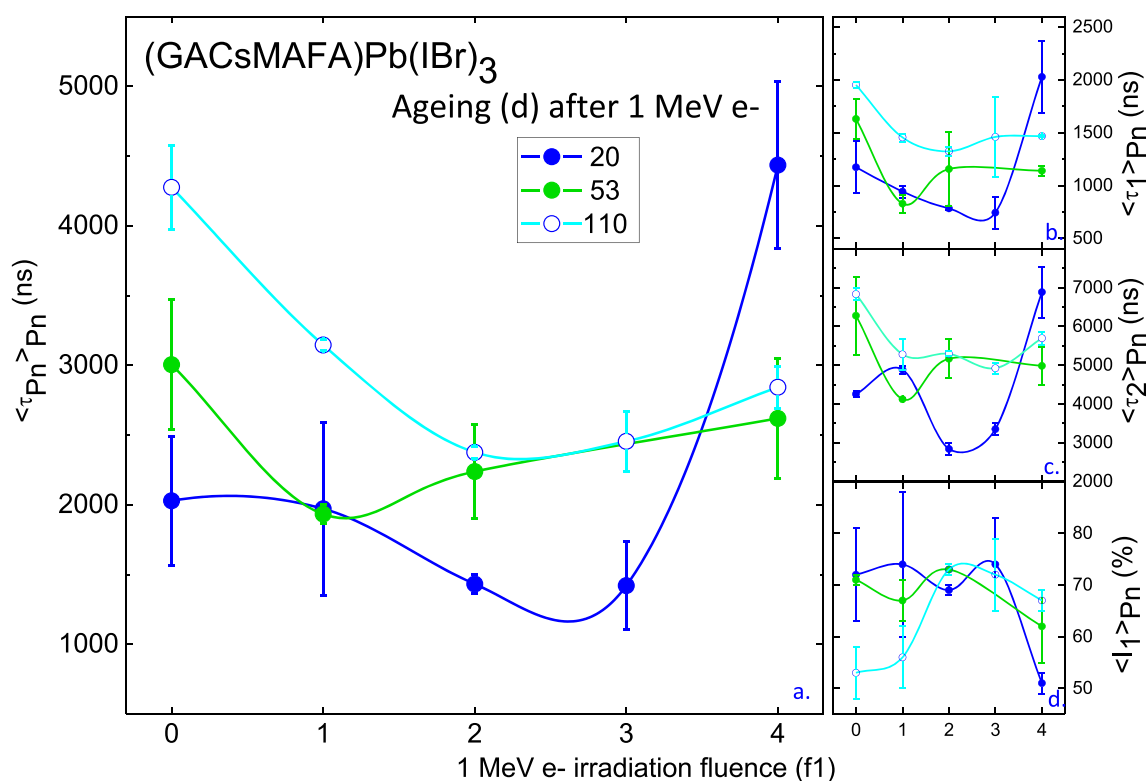


Fig. 7 Fluence dependence of the average lifetime decay spectra recorded after aging and 30 min of laser illumination (Fig. 5) in (GACsMAFA)Pb(IBr)₃ HOIPs for the Ajd-rf-f0 reference layer and the Ajd_fn 1 MeV e-irradiated layers at the fn fluence. The conditions for the

Ajd aging are j(d) = 20/53/110 under N₂ atmosphere in dark at ~300 K. The TRPL spectra are recorded using a nano-LED_482nm, 14 pJ/pulse energy, 100 ps pulse duration, and 10 kHz repetition rate. The laser spot has a diameter of about 250 μ m diameter

Irradiation versus native defects: effect on A0d optical absorption This paragraph shows that there are shallow and deep A0d localized electronic states in the 7d aged A0d_rf-f0 and 1 MeV e-irradiated A0d_fn layers. The populations of A0d defects that are respectively associated to these distributions are modified by the 1 MeV e-irradiation. The concentration/nature of the A0d defect populations and their contribution to the A0d localized electronic states evolve with the A0d_fn-c_{ir} concentrations of irradiation defects.

Native defects in the 7d aged A0d_rf-f0 reference layer The energy-dependence of the absorbance in the A0d_rf-f0 reference layer corresponds to a layer that has aged 7d in dark under N₂ atmosphere at room temperature (N₂, dark, ~300 K). This energy-dependence displays the typical shape reported for similar quadruple cation based HOIPs [4, 5]. For the thickness of the layer, d = 500 nm, the absorption coefficient, $\alpha(E)$, has a value in cm⁻¹: $\alpha(E) = 4.61 \cdot 10^4 A(E)$ (Fig. 2). At 2 eV, the value $\sim 8 \cdot 10^4$ cm⁻¹ is quite consistent with those found for example in MAPbI₃ [13, 17, 19] and of the same order as those in other semiconductors used in photovoltaic applications. This shows that the 7d aging has little effect on the absorption coefficient in the higher energy range $E(\text{eV}) \geq 1.68$.

As determined in Sect. 3, the optical bandgap at room temperature in A0d_rf-f0 has a value A0d_rf-f0_Eg-300K in eV of

1.63(1) (Table 2). In A0d_rf-f0, the onset for the optical transitions is $\sim 1.56(1)$ eV. The absorption edge has a width where the logarithm of the absorbance increases linearly as the energy increases up to $\sim 1.68(1)$ eV (Fig. 1). This corresponds to an exponential smearing of the absorption coefficient (Fig. 1), $\alpha(E) = \alpha^0 \cdot \exp((E-E^0)/E_U(T(K)))$ with an Urbach energy ([20] and references herein), $E_U(T(K))$, characteristic of the energy width of the absorption edge. The Urbach energy in the A0d_rf-f0 reference layer has a value in meV, A0d_rf-f0-Eu-300K-52(2) (Table 4). This value in A0d_rf-f0 can be compared to the value determined in a pristine layer prepared in the same way as rf-f0 and rf-17. The energy-dependence of the absorbance determined in this layer via photothermal deflection spectroscopy (PDS) measurements at room temperature in perfluorinated liquid yields a value of 1.64(1) eV for the bandgap and of $\sim 18(2)$ meV for the Urbach energy. The value for the bandgap is quite consistent with that in A0d_rf-f0. The value for the Urbach energy is significantly lower than in A0d_rf-f0.

The 7 days aging (N₂, dark, ~300 K) appears to have little effect on the bandgap value while it affects the Urbach energy in the GA_{0.015}Cs_{0.046}MA_{0.152}FA_{0.787}Pb(I_{0.815}Br_{0.185})₃ layers. The bandgap values in these layers are slightly higher, $\geq 0.03(1)$ eV, than those reported in layers prepared from precursor solutions with different relative molarities as concern the mixing of the four cations as well as of the halide anions

[4, 5]. In [4], GA cations were gradually incorporated in $\text{Cs}_{0.1}(\text{FA}_{0.83}\text{MA}_{0.17})_{0.9}\text{Pb}(\text{I}_{0.83}\text{Br}_{0.17})_3$ perovskite films deposited on glass/ITO substrates. The GA content in the CsMAFA precursor solutions was varied by adding GAPbI_3 with increasing molar ratio from 10% to 40%. The bandgap energy was found at around 1.61 eV independently on the amount of GA addition in the precursor solutions. In [5], $\text{Cs}_{0.05}(\text{FA}_{0.83}(\text{MA}_{1-x}\text{GA}_x)_{0.17})_{0.95}\text{Pb}(\text{I}_{0.83}\text{Br}_{0.17})_3$ perovskites films on glass/FTO substrates were characterized as a function of the MA to GA cation stoichiometry. Layers were prepared from different precursor solutions where GA cations gradually replace MA cations. In this case, the optical bandgap energy value increases with increasing GA stoichiometry, from 1.60 eV for $x = 0.1$ to ~ 1.63 eV for $x = 0.6$. From DFT calculations, it is generally the PbX_6 octahedra that are considered as the main factor determining the bandgap value [2, 21]. The size of the cations on the A-sites of the APbX_3 perovskites can however either contract or expand the crystal lattice, thereby altering the optical bandgap [22]. The small differences in the bandgap values reported by [4, 5] with those reported here may rather be ascribed to the slight differences in the halide anion stoichiometry.

The exponential increase of the absorbance at the absorption edge is related to the existence of transitions involving electronic states lying in tails of the density of states in the valence and conduction bands (band tails) ([20] and references herein). The existence of native near-band edge electronic states has already been reported for HOIPs. From external quantum efficiency (EQE) measurements at the absorption edge, an Urbach energy of 16(1) meV is derived for the active MAPbI_3 layers in n-i-p or p-i-n solar cells, independently on the preparation procedure—vapor deposition growth or coating from solutions [23]. The presence of band tails in pristine FAPbI_3 was also inferred from the PL temperature-dependence [24]. The authors report the presence of two peaks in the PL spectra obtained at low-temperature PL measurements performed at increasing illumination intensity. The higher energy peak with increasing temperature displays a blue-shift to higher energy. On the contrary, the lower energy peak with increasing temperature exhibits a redshift. The blue-shift is the usual behavior observed in HOIPs ([24] and references herein). It was attributed by Wright et al. to the radiative recombination of electron-hole delocalized in the conduction-valence bands and identified as excitons from 10 to 50 K in FAPbI_3 . The lower peak was related to trap mediated radiative emission.

The 7 days aged A0d_rf-f0 reference layer (7d, N_2 , dark, ~ 300 K) has a much larger Urbach energy than the pristine rf-17 layer, by about a factor ~ 3.3 . It follows that the tail distribution of shallow localized electronic states is broader in A0d_rf-f0 than in rf-17. The question is whether this difference reflects uncontrolled variability in the layer preparation and/or the 7d aging. One notices that the bandgap in the

pristine layer prepared with the same procedure as rf-17 and A0d_rf-f0 , 1.64(1) eV, is in excellent agreement with the 1st PL peak energy in the pristine rf-17 layer, 1.6426(5) eV. This strongly supports that the 7d aging rather than variability during layer preparation plays a dominant role in the broadening of the band tails. This broadening indicates an increase of the concentration of the defects that give rise to the shallow localized electronic states in the bandgap tail. The question is whether these 7d aging-induced defects in the A0d_rf-f0 reference layer have the same nature as those that are generated during the preparation. One possibility is that the interaction between the layer surface and the N_2 atmosphere induces structural disorder (vacancies, interstitials, dislocations, site substitutions) or compositional one (deviation from stoichiometry, doping) that are rather specific to the (N_2 , dark, ~ 300 K) aging processes than to the preparation.

At higher and lower energy than the absorbance edge, the A0d_rf-f0 reference layer absorption coefficient varies slowly in A0d_rf-f0 . The ratio of its values in the lower range to the higher energy range mainly reflects the height of the absorbance steep step. For example, as energy decreases from 2 to 1.2 eV, the absorption coefficient decreases by factor $\alpha_{\sim 300\text{K}}(1.2)/\alpha_{\sim 300\text{K}}(2) \sim 1.1 \times 10^{-1}$. This factor is much smaller than in the pristine layer prepared in the same condition as A0d_rf-f0 and rf-17. The ratio between the two values is in this layer, $\sim 8.2 \times 10^{-4}$. Such variations are also observed in other HOIPs. For example, the ratio for $\alpha_{\sim 300\text{K}}(1.53)/\alpha_{\sim 300\text{K}}(1.7)$ as energy decreases from 1.7 to 1.53 eV are in MAPbI_3 about $\sim 10^{-2}$ [13] or 2.5×10^{-3} [25], and for example $\sim 1.3 \times 10^{-1}$ in $\text{Cs}_{0.17}\text{FA}_{0.83}\text{Pb}(\text{Br}_{0.2}\text{I}_{0.8})_3$ [18], respectively.

Below the absorption edge, for $1.2 \leq E(\text{eV}) \leq 1.6$, the A0d_rf-f0 reference layer absorption coefficient slowly decreases with decreasing energy towards mid-gap and, as seen above, its values remain quite high compared to those in the higher energy range above the absorption edge. This indicates that, beyond the absorption onset towards mid-gap, there is a A0d_rf-f0 distribution of deep localized electronic states. This distribution is present in the 7 days aged A0d_rf-f0 layer and absent in the pristine one. It reflects the differences in the layer quality as concern structural and compositional disorders. Distributions of deep electronic states have also been observed in MAPbI_3 layers [13, 23]. More generally, in semiconductors, defects giving rise to localized electronic states lying deep in the forbidden gap may modify the sub-band optical behavior [26]. One of the known examples is the native defect energy level known as EL2 in GaAs [27]. This localized energy level is located at 0.75 eV below the conduction-band extremum. When the EL2 defects are present, this level can completely dominate the sub-bandgap absorption at 10 K. Another example for amorphous silicon deposited on sapphire (SOS) is the effect on absorption of ion implantation [28]. The authors report the existence of some new features that appear after implantation in the subgap region of absorption at 300 K.

The authors attribute them to the formation of divacancy defects in ion-implanted amorphous silicon. Another effect is that ion-implantation induced an increase of the absorption coefficient in the sub-band region. This absorption increase is attributed to the formation of a damaged crystalline silicon or a co-existence of amorphous and crystalline damaged silicon phases.

In summary, the 7d aging (N_2 , dark, ~ 300 K) in the $GA_{0.015}Cs_{0.046}MA_{0.152}FA_{0.787}Pb(I_{0.815}Br_{0.185})_3$ A0d_rf-f0 reference layer generates “native” 7d aging-induced defects that give rise to A0d_rf-f0 deep localized electronic states. Defects that generate A0d_rf-f0 shallow levels are also introduced. On the basis of the absorbance, it is difficult to determine whether the 7d aging-induced A0d_rf-f0 shallow defects have the same nature as those present in a pristine layer or are different.

Irradiation versus native defects in the A0d_fn layers aged 7d before irradiation

In the irradiated A0d_fn layers, it is assumed that the 7d aging before irradiation induces native 7d aging-induced defect populations similar to those present in the A0d_rf-f0 reference layer. The absorption coefficient in the higher energy range above absorption edge, $\sim 1.68 \leq E(\text{eV}) \leq 2.12$ eV, and the bandgap remain independent on fluence in the A0d_fn layers (Table 2). For both, the values in the irradiated A0d_fn layers are the same as in the A0d_rf-f0 layer. This is a clear evidence that 1 MeV e-irradiation at fluences, $f1 \leq fn \leq f4$, introduces irradiation defect populations with A0d_fn-c_{ir} concentrations low enough to preserve the layer composition stoichiometry and crystalline structure that exist in the A0d_rf-f0 layer.

There is an exponential smearing of the absorption edge in the irradiated A0d_fn layers that yields to fluence dependent Urbach energies (Table 4). The values are in meV, A0d_fn- $E_{u \sim 300K}$: $f1$ - $f2$ - $f3$ -47(2); $f4$ -50(2). When compared to the value in A0d_rf-f0 reference layer, 52(2) meV, the width of the A0d_fn band tails goes through a weak minimum as the concentration of irradiation defects increase in the range $f1 < fn \leq f3$. This minimum suggests the A0d_fn tails of shallow localized electronic states evolve with the irradiation defects according to different modes depending on their A0d_fn-c_{ir} concentration. The A0d_f1-c_{ir} concentration of irradiation defects appears to be sufficient to slightly reduce the width of the initial band tails. The irradiation defects seem to partially remove the initial native ones. As fluence increases further, it is only the higher A0d_f4-c_{ir} concentration of irradiation defects that appears to be sufficient for contributing also to the band tails and to broaden their distribution.

In the lower energy range below the absorption onset, $1.2 \leq E(\text{eV}) \leq 1.6$ eV, the absorption coefficients in the irradiated A0d_fn layers have a slow decrease towards mid-gap and have still high values. For example, the value at 1.2 eV is only one order of magnitude less than at 2 eV. This shows the existence of electronic states in the sub-bandgap region which

extends towards mid-gap. The baseline of the absorption coefficient reaches a minimum with increasing fluence for $f3$. This indicates that the initial sub-bandgap distribution of electronic states below 1.6 eV present in the reference A0d_rf-f0 layer is affected by the introduction of irradiation defects. The A0d_fn irradiated layers are more transparent than the reference A0d_rf-f0 one. This suggests that irradiation reduces the density of the “native” 7d aging-induced deep electronic states or affects the absorption oscillator strength by changing their nature. In the first case, the role of the irradiation defects in A0d_fn implies a destruction of the initial deep electronic states observed in A0d_rf-f0. In the second case, it implies a progressive replacement of those with irradiation-induced deep electronic states. The competition between these two processes can explain why the absorbance in the lower energy region goes through a minimum for the $f3$ fluence. As fluence increases up to $f2$, the predominant role of the irradiation defects is to progressively remove the contribution of the native deep electronic states to the optical absorption. At $f3$, the concentration of irradiation defects, A0d_f3-c_{ir}, reaches a threshold value sufficient for partially removing the initial deep electronic states defects in A0d_rf-f0. The absorbance for $f3$ then goes through a minimum. Above the $f3$ fluence, as the concentration further increases to A0d_f4-c_{ir}, their role as producing deep electronic states within the bandgap becomes predominant. It is reflected by the absorbance increase as fluence increases from $f3$ to $f4$.

The absorbance oscillations in the energy region $1.2 \leq E \leq 1.6$ eV have amplitudes that are higher in the irradiated A0d_fn layers than in the reference A0d_rf-f0 one. In the case of thin layers/films on thick substrates, oscillations may appear in the transmission and reflection spectra that arise from interference fringes produced at the interface between the layer/film and its substrate [29]. The stronger amplitude of the oscillations in the A0d_fn layers suggests that roughness is stronger in A0d_fn than in A0d_rf-f0 [30].

In summary, for the 1 MeV electron irradiation conditions chosen in this work, the fluence effects observed for the A0d absorbance in the (GACsMAFAPb)(IBr)₃ layers set-18 are fully consistent with the existence of distributions of shallow and deep sub-bandgap electronic states. The density and/or the nature of the localized states change with the concentration of irradiation defects in the A0d_fn layers. At the low A0d_fn-c_{ir} concentrations in the fluence range $f1 \leq fn \leq f3$, the irradiation defects most likely decrease the density of the shallow and deep electronic states initially present. Their main role is then to partially remove the native 7d aging-induced defects that give rise to the initial distributions, i.e., the defects that exist after the (7d, N_2 , dark, ~ 300 K) initial aging. At the higher A0d_f4-c_{ir} concentration, for the $f4$ fluence, their main role is to introduce shallow and deep localized electronic states that differ from the initial ones.

Electron irradiation induced-aging of optical absorption

Absorbance gives access to four types of variations that can be examined to determine how the initial 7d aging-induced defects evolve with aging duration in the A_{jd_rf-f0} reference layer and interact with the irradiation defects in the 1 MeV e-irradiated A_{jd_fn} layers ($j(d) = 53, 110$). These variations are those of (i) the bandgap, (ii) the Urbach energy, (iii) the energy dependence of the absorption coefficient in the higher energy range above the absorption edge, $E(eV) \geq 1.68$, and (iv) the energy dependence of the absorption coefficient in the lower energy range below the absorption edge, $E(eV) \leq 1.6$.

Aging-induced defects in the A53d/A110d_rf-f0 layer

The main effect of increasing the aging duration in the A53d/A110d_rf-f0 layer is to induce variations of the (ii) and (iii) types. (ii) The increase of aging duration produces a distribution of shallow electronic states that slightly broadens as aging duration after preparation increases from 7d(A0d) to 60d(A53d), and further, till 117d(A110d). (iii) In the higher energy range above the absorption edge, $E(eV) \geq 1.68$, the aging between 7d(A0d) to 60d(A53d) induces a decrease of the absorption coefficient that is much stronger above $E(eV) \geq 2.2$ than below. The further aging from 60d(A53d) to 117d(A110d) has a much smaller effect. It only slightly decreases the absorption coefficient. It follows that the increase of aging duration after preparation to 60d(A53d) and further, till, 117d(A110d) introduces two kinds of A_{jd_rf-f0} aging-induced defects population. The first kind rather affects the shallow localized electronic states. The second one rather affects the absorption coefficient in the higher energy range above the absorption onset.

Irradiation induced-aging defects in the A53d/A110d_fn layers

The concentration of irradiation defects, $A_{0d_fn-c_{ir}}$, introduced in the A_{0d_fn} layers induces variation of the four types as aging duration after irradiation increases up to 53d(A53d) and 110d(A110d). (i) The optical bandgap in the A53d/110d_fn irradiated layers depends on the fn fluence. Compared to the respective values in A53/A110d_rf-f0 reference layer, it has a systematic tendency to slightly shrink as the irradiation defect concentration reaches a threshold value corresponding to the f2 fluence. The irradiation-induced bandgap narrowing for $f2 \leq fn \leq f4$ depends on the aging duration and has values in eV, $A_{jd_fn-dE_{-300K}}$: A53d_f2-f3-f4(-0.02(2)); A110d_f2(-0.02(2)), A110d_f3-f4(-0.03(2)). (ii) The absorbance exhibits an energy exponential dependence in the steep part at the absorption edge of the A53/A110d_fn layers. The associated A_{jd_fn} Urbach energy in the A53d/A110d_fn layers goes through a maximum as the $A_{0d_fn-c_{ir}}$ irradiation defect concentration increases with increasing fluence. The maximum for both aging durations is reached for the $A_{0d_f2-c_{ir}}$ defects concentration produced at the f2 fluence (Table 4). The maximum value of the A_{jd_f2}

Urbach energy at f2 increases with aging duration and has values in meV, $A_{jd_f2-E_{u-300K, max}}$: A53d_f2-83(2), A110d_f2-100(2). (iii) In the higher energy range above the absorption edge ($E(eV) \geq 1.68$), the absorption coefficient decreases with increasing $A_{0d_fn-c_{ir}}$ irradiation defect concentration. The decrease is stronger above $E(eV) \geq 2.2$ than below. Furthermore, it reaches a saturation level at each A53d/110d aging as the A_{0d_fn} irradiation defects reaches a concentration threshold, $A_{0d_f2-c_{ir}}$, corresponding at the f2 fluence. (iv) In the lower energy range below the absorption edge, $1.2 \leq E(eV) \leq 1.6$, the A53d/A110d absorbance depends on the $A_{0d_fn-c_{ir}}$ concentrations of irradiation defects. As aging duration increases, 47d(A110d-A53d), the A_{jd_fn} layers absorption increases in this energy region. At each A53d/A110d aging, the most absorbing A_{jd_fn} layers correspond to the $A_{0d_f1-c_{ir}}$ and $A_{0d_f2-c_{ir}}$ irradiation defect concentrations introduced at the f1 and f2 fluences, respectively.

Irradiation induced-A53d/A110d aging processes

When the effects of increasing aging duration are compared for the absorbance in the irradiated A_{jd_fn} and the reference A_{jd_rf-f0} layers, there is clear evidence that the A_{0d_fn} irradiation defects affect the 53d/110d aging processes. The $A_{0d_f2-c_{ir}}$ concentration of irradiation defects introduced at the f2 fluence in the A_{0d_f2} layer appears as a threshold. At this threshold concentration, the aging processes in the f2 layer (i) start to shrink the A53d/A110d_fn bandgaps and (ii) produce A53d/A110d_fn band tails with a maximal width. The width is about 36–40% larger in the A53d/A110d_f2 layer than in the A53d/A110d_rf-f0 reference one. At this threshold concentration, the aging processes (iii) cease to affect the A53d/A110d_fn absorption coefficients in the higher energy range above the absorption edge. At this threshold concentration, the aging processes (iv) induce the higher A53d/A110d_fn subgap absorbance. These correlated effects lead to conclude that the irradiation-aging induced defect populations differ below and above the $A_{0d_f2-c_{ir}}$ irradiation defect concentration. Depending on the balance between the competitive chemical reactions occurring during aging, the concentration and/or the nature of the shallow and deep localized electronic states change below and above this threshold concentration.

In summary, the energy-dependence of absorbance in the A_{jd_rf-f0} reference layer has a ($j(d), N_2$, dark, ~ 300 K) aging-induced evolution that leads to identify three different kinds of A_{jd_rf-f0} defect populations. One kind (i) induces a slight A_{jd_rf-f0} bandgap shrinkage and, consequently, corresponds to a high aging-defect concentration, $A_{jd_rf-f0_c1_{ag}}$. The two others (ii) and (iii) generate shallow and deep A_{jd_rf-f0} electronic states, respectively. The concentration associated to the shallow ones is so high that the states overlap and give rise to a quasi-continuous distribution of energy levels in the A_{jd_rf-f0} band tails.

The energy-dependence of absorbance in the A_{jd_fn} irradiated layers has a (N_2 , dark, ~ 300 K) aging-induced

evolution consistent with the existence of three types of Ajd_{fn} defect populations that generates (i) Ajd_{fn} bandgap shrinkage, (ii) shallow and (iii) deep Ajd_{fn} electronic states, respectively. None of the three irradiation-aging induced populations displays a monotonous evolution as a function of the irradiation defects concentrations ($A0d_{fn-c_{ir}}$) with increasing aging. The three types of (i)-(iii) irradiation-induced aging populations in the Ajd_{fn} irradiated layers differ by their concentration and/or nature from the aging-induced ones in the Ajd_{rf-f0} reference layer. The increase of aging duration tends to systematically increase the contribution of the Ajd_{fn} deep electronic states to the Ajd_{fn} sub-bandgap absorbance.

Natural and irradiation-induced-aging defects: PL after 1–3 min of illumination (454 nm, 1.1 W/cm², air, ~ 300 K)

When illumination starts in the aged Ajd ($j(d) = 20, 53, 110$) $rf-f0$ reference and 1 MeV e-irradiated fn layers, as discussed above, three types of irradiation aging-induced Ajd defects are initially present. The first one induces the slight bandgap Ajd_{fn} shrinkage that depends on aging and fluence. The second one generates the Ajd band tails of shallow electronic states. The third one gives rise to the Ajd sub-bandgap distributions of deep electronic states. For the 20d aged states of the layers, the properties of these distributions are inferred from those in the $A0d$ and $A53d$ aged states. As a result of the “native” Ajd aging-induced distributions, the Fermi level position in dark can vary in the Ajd_{rf-f0} and Ajd_{fn} layers. Under illumination, the electron and hole quasi-Fermi level respective positions may also depend on the layer states ([31] and references herein). Furthermore, the elimination of the metastable $A0d_{fn}$ irradiations defects in the Ajd_{fn} layers can have properties that differ under illumination from those in dark. The reason is that the defect migration energy and the rates of the chemical reactions involving the defects are expected to depend on the occupancy of the defect charge states. Those occupancies are controlled by the respective positions of the defect ionization levels and of the Fermi level in dark or those of the electron and hole quasi-Fermi levels under illumination.

For the $A20d$ aging, the values for the $A20d_{fn}$ bandgap shrinkage are expected between those for the $A0d_{fn}$ and $A53d_{fn}$ ones (Table 2). For the shallow electronic states, the Urbach energies associated to the $A20d_{fn}$ near bandgap distributions are inferred from the values determined for the $A0d$ and $A53d$ ones (Table 4). For the $A20d_{rf-f0}$ reference layer, the value is most likely equal to their average, 53(2) meV (Table 4). For the irradiated $A20d_{fn}$ layers, it seems reasonable to assume that the $A20d_{fn}$ Urbach energies are for each fn fluence between the $A0d_{fn}$ and $A53d_{fn}$ values (Table 4), respectively. The indetermination of the value covers an order of magnitude as the concentration of irradiation defects increases with increasing fluence from $f1$

to $f4$. This indetermination is minimal for the fluence $f1$, 3(50–47) meV. It goes through a marked maximum for the fluence $f2$, 36(83–47) meV. Then, as the irradiation defect concentrations increases further at higher fluence, the range of indetermination becomes quasi-constant and, about, twice less than at $f2$ with values for $f3$ -14(61–47) meV and $f4$ -17(67–50) meV.

For the deep electronic states, their $A20d$ sub-bandgap distribution is expected to affect the energy dependence of the absorption coefficient in the $A20d_{rf-f0}$ reference and $A20d_{fn}$ irradiated layers and induce variations between those due to the $A0d$ and $A53d$ sub-bandgap distributions. For all the fluences, except $f2$, these distributions are expected to be less absorbent in the $A20d_{fn}$ layers than in the $A20d_{rf-f0}$ one. There is an indetermination for the $f2$ fluence. The question is whether the sub-bandgap distribution during the 20d aging remains less or becomes more absorbent in $A20d_{f2}$ than in $A20d_{rf-f0}$. Indeed, from less absorbent in the $A0d_{f2}$ state than in $A0d_{rf-f0}$, the distribution becomes more absorbent in the $A53d_{f2}$ one than in $A53d_{rf-f0}$.

First PL spectra in the pristine $rf-17$ and aged Ajd_{rf-f0} layers

For the pristine $rf-17$ layer, the 1st PL spectrum recorded after 1 min of 488 nm illumination in air can be considered as defining the quality of the pristine state of a (GACsMAFA)Pb(I_{Br})₃ layer. For the layer set-18, the 1st PL spectra are recorded after 3 min of 454 nm illumination in air. These spectra in Ajd_{rf-f0} define the quality of a layer where processes occurring during (N₂, dark, ~ 300 K) aging after preparation are coupled to those occurring during 3 min illumination at 454 nm in air performed after each aging period. One question is whether the radiative recombination in the pristine $rf-17$ and aged Ajd_{rf-f0} reference layers involves only band-to-band carrier recombination or involves also radiative recombination via carrier traps.

The difference between the values of the bandgap and 1st PL peak energy depends on the layer state (Table 5). For the pristine state, there is an excellent agreement between those two values, 1.64(1)eV in the pristine layer -prepared as $rf-17$ - and the 1st PL peak recorded in $rf-17$ after 1 min of illumination, 1.6426(5) eV. This suggests that it is rather band-to-band radiative recombination that takes place in the pristine $GA_{0.015}Cs_{0.046}MA_{0.152}FA_{0.787}Pb(I_{0.815}Br_{0.185})_3$ $rf-17$ layer. In the aged Ajd_{rf-f0} reference layer, the energy differences, Ajd_{rf-f0} - [Eg-Ep(1st)], remain quasi-constant ~ 0.04(1) eV as the aging duration increases (Table 5). This is independent of the tendency (at the limit of detection) for the bandgap to shrink by -0.02(2) eV in Ajd_{rf-f0} during the 110d aging from $A0d$ to $A110d$. The differences are slightly smaller, by ~ 10–20 meV, than the initial Urbach energy for the Ajd_{rf-f0} : $A0d/53d/100d_{rf-f0-Eu-300K-52/53/59(2)}$. In addition, there is no correlation with increasing aging between the variations of the 1st PL peak energy and FWHM in the reference Ajd_{rf}

Table 5 Difference between the first photoluminescence peak and bandgap energy after aging in (GACsMAFA)Pb(IBr)₃ HOIPs for the reference Ajd_rf-f0 and the 1 MeV e-irradiated Ajd_fn layers at the fn

(Ep(Ajd_fn)-Eg(Ajd_fn)) (eV)	rf-f0	f1	f2	f3	f4	vsf0_f1	vsf0_f2	vsf0_f3	vsf0_f4
Ep(A20d)-Eg(A0d)	-0.04(1)	-0.04(1)	-0.04(1)	-0.04(1)	-0.06(1)	0.00(2)	0.00(2)	0.00(2)	-0.02(2)
Ep(A53d)-Eg(A53d)	-0.04(1)	-0.04(1)	-0.02(1)	-	-0.03(1)	0.00(2)	0.02(2)	-	0.01(2)
Ep(A110d)-Eg(A110d)	-0.04(1)	-0.03(1)	-0.03(1)	-0.01(1)	-0.01(1)	0.01(2)	0.01(2)	0.03(2)	0.03(2)
vsA0d_A53d	0.00(2)	0.00(2)	0.02(2)	-	0.03(2)				
vsA0d_A110d	0.00(2)	0.01(2)	0.01(2)	0.03(2)	0.05(2)				
vsA53d_A110d	0.00(2)	0.01(2)	0.01(2)	-	0.02(2)				

fluence. The conditions for the Ajd aging are $j(d) = 0/20/53/110$ under N₂ atmosphere in dark at ~300 K

f0 layer. The Ajd_rf-f0 1stPL peak FWHM goes through a maximum after the A53d aging while the Ajd_rf-f0 1st PL peak energy goes on decreasing. This reflects that the Ajd_rf-f0 1st PL spectra are composed of overlapping shallow emission transitions that evolve towards lower energies with increasing aging in the Ajd_rf-f0 reference layer. Given the Ajd_rf-f0 1st PL characteristics, the conclusion is that radiative carrier recombination in Ajd_rf-f0 involves shallow energy levels after each Ajd aging.

For most inorganic semiconductors, the broadening of a PL peak may depend on several factors, notably scattering with defects (imperfections, disorder...) as well as electron-phonon coupling [32, 33]. In pristine HOIPs -MAPbI₃, MAPbBr₃, FAPbI₃, FAPbBr₃- layers deposited on quartz substrates, FWHM was extracted from temperature-dependent steady-state PL under vacuum and compared with the emission broadening estimated from DFT and many-body perturbation theory calculations [32]. This broadening was found to mainly arise from the sum of the impurity scattering term and electron-optical phonon scattering. The first term is temperature independent. The second one increases linearly with increasing temperature. At room temperature, the extracted FWHM values in vacuum vary between 0.09 and 0.11 eV and are shown to be in good agreement with the DFT calculations. The values reported in [32] are consistent with those found for the first PL spectra in the pristine rf-17 layer, 0.099(1) eV, and in the aged reference Ajd_rf-f0 layer spectra, between 0.110(4) and 0.113(4) eV in (air, 300 K).

The shallow trap-assisted carrier radiative recombination in the aged reference Ajd_rf-f0 layer has the interesting property that the Ajd_rf-f0 1st PL peak intensity goes through a minimum at A53d. The shallow electronic levels under illumination have an ability to participate to radiative recombination that slightly decreases (-10%), during the first 33d(A20d-A53d) aging period. This ability is so much restored during the second 47d(A53d-A110d) one that the 1st PL peak intensity becomes 80% higher in A110d_rf-f0 than in A20d_rf-f0. This evolution is singular when compared to the broadening of the initial Ajd near bang gap tails, 1 meV from A20d to

A53d and 6 meV from A53d to A110d. The assumption that the initial Ajd_rf-f0 aging-induced shallow electronic levels directly play a role implies that the 6 meV broadening increases the probability of radiative recombination under 3 min of illumination by 90% from A53d_rf-f0 to A110d_rf-f0. It also implies that the 6 meV broadening results in the associated decrease of the 1st PL peak energy of approx. -0.010 eV. It seems rather difficult to attribute such effects to the 6 meV broadening. Consequently, this questions the direct role of the initial Ajd_rf-f0 aging-induced shallow electronic levels on the radiative recombination in the Ajd_rf-f0 layer. The initial Ajd_rf-f0 aging-induced deep sub-bandgap electronic levels are potential non-radiative recombination centers that, depending on the occupancy of their ionization levels under illumination, can affect the Ajd_rf-f0 1st PL intensities. On the basis of the quasi-absence of variation of the sub-bandgap absorption during the 47d(A53d-A110d) second aging period, they appear to remain rather stable during this second period. For them to be at the origin of the huge difference (90%) between the A53d and A110d_rf-f0 1st PL intensities requires that their occupancy is totally different under illumination performed in the aged reference Ajd_rf-f0 layer after the A53d/A110d aging. Such a property seems to be unlikely and, consequently, questions their direct role.

In summary, the features of the evolution of the Ajd_rf-f0 1st PL peak characteristics with increasing aging in the Ajd_rf-f0 reference layer lead to the conclusion that most likely the first 3 min of illumination already affects both Ajd_rf-f0 distributions of shallow and deep electronic levels. One notices that this is also the case in the pristine layers (Fig. 4) when one compares the initial Urbach energy (18 meV) and initial absence of deep subgap states with the PL evolution in rf-17. Between the 3rd and 1st PL spectra in rf-17, the 3 min instead of 1 min of illumination already induces a decrease of approx. -0.026 meV and approx. -30% for the energy and intensity, respectively. The nature and density of those illumination-induced defect populations may differ in the Ajd_rf-f0 aged reference layer and the rf-17 pristine one, depending on the chemical reactions that are initiated and

promoted under 454 nm \sim 300 K illumination in air by the initially different defect populations.

First PL spectra in the irradiated and, subsequently, aged Ajd-fn layers

The aging dependence of the 1st PL spectra in the irradiated Ajd_{fn} aged layers is clearly affected by the A0d_{fn-c_{ir}} irradiation defect concentrations. After 3 min of illumination, the Ajd_{fn}-1st PL spectra have emission characteristics (energy, FWHM, intensity) that are controlled by the under-illumination occupancy of the electronic levels. In the Ajd_{fn} layers, there exist different types of initial electronic levels: (i) the delocalized ones in the conduction/valence bands and, in addition, depending on the A0d_{fn-c_{ir}} irradiation defect concentrations, those (ii) localized at irradiation-aging defects and those (iii) partially or fully delocalized in irradiation-aging defect bands.

One question is whether the introduction of the A0d_{fn-c_{ir}} of the irradiation defects promotes radiative recombination via band-to-band or carrier traps in the Ajd_{fn} aged irradiated layers. One can examine how the difference between the 1st PL peak energy and the bandgap values, Ajd_{fn}-[Eg-Ep(1st)] (eV), evolves with the A0d_{fn-c_{ir}} concentration of irradiation defects to determine which radiative process is the most probable. Table 5 shows that the emission energy is lower than the bandgap for every aging duration and fluence. The energy emission is the less different from the bandgap, approx. -0.01 eV, for the A110d aging and the higher A0d_{fn-c_{ir}} concentrations of irradiation defects at the f3-f4 fluences. In this case, given this low value, the possibility that the emission corresponds to a band-to-band radiative recombination cannot be totally excluded. Otherwise, the large shifts for the other aging periods and irradiation defect concentrations, approx. -0.06 to approx. -0.02 eV (Table 5), suggest that the radiative carrier recombination remains assisted by shallow carrier traps.

The detailed examination of the Ajd_{fn}-1st PL spectra shows that the A0d_{fn-c_{ir}} irradiation defect concentrations induces no simultaneous monotonous variations of their characteristics - peak energy, FWHM and intensity. There are however some key trends (i)–(vi) worth noting between their evolution with increasing Ajd aging:

- (i) The Ajd_{f1}-PL(1st) spectra for the lower A0d_{f1-c_{ir}} concentration have energy and FWHM values that are always the higher ones.
- (ii) There is an absence of correlation between the Ajd_{fn}-Ep(1st) peak energy and initial Ajd_{fn} Urbach energy variations with increasing Ajd aging.
- (iii) The irradiation-induced dispersion of the Ajd_{fn}-1st PL peak energy and FWHM goes through a minimum after the A53d aging.
- (iv) For A20d, the A20d_{fn}-Ip(1st) intensity decreases with increasing concentration of irradiation defects:

$$A20d_{f1}-Ip(1st) \sim (-20\%) > A20d_{f2}-Ip(1st) > A20d_{f3}-Ip(1st) >> A20d_{f4}-Ip(1st) \sim (-60\%).$$

- (v) The irradiation-induced dispersion of the Ajd_{fn}-Ip(1st) intensities goes on decreasing with increasing aging.
- (vi) Except for the Ajd_{f1} layer, the Ajd_{fn}-1st PL intensity increases with increasing A20d to A110d aging. This property becomes also true in the Ajd_{f1} layer with increasing A53d to A110d aging.

The trend (i) indicates that the main A20d_{fn} emission transitions involve ionization levels that are the shallower ones at the lower irradiation defects concentration, A0d_{f1-c_{ir}}. The trend (ii–iii) suggest that the emission transitions due to shallow levels are not directly imposed by change in the occupancy of the electronic levels arising from the initial irradiation-aging near band edge distributions. It rather seems to indicate that illumination generates specific distributions of shallow levels. The trend (iv) shows that the concentrations of A20d_{fn} non-radiative recombination centers active under illumination increase with the A0d_{fn-c_{ir}} concentrations. The trend (v) shows that the effects of the A0d_{fn-c_{ir}} irradiation defect concentrations on the Ajd_{fn} non-radiative recombination centers active under illumination decrease with increasing Ajd aging duration. The trend (vi) appears to occur when the aging-induced Ajd_{fn} bandgap shrinkage yields in the Ajd_{fn} layers to bandgap values in eV, Ajd_{fn}(Eg) $\leq 1.61(1)$.

In summary, when the 3 min (454 nm, air, \sim 300 K) illumination effects are compared in the Ajd_{fn} irradiated layers and the Ajd_{rf-f0} reference one, the most obvious differences concern the Ajd_{fn}-PL(1st) intensities. The ratios Ajd_{fn}-Ip(1st)/A20d_{rf-f0}-Ip(1st) and the ratios Ajd_{fn}-Ip(1st)/Ajd_{rf-f0}-Ip(1st) at each aging are systematically lower than 1. This is clear evidence that the combination of irradiation-induced aging (N₂, dark, \sim 300 K) and 3 min of 454 nm illumination systematically yields to concentrations of non-radiative recombination centers always higher under illumination in the Ajd_{fn} irradiated layers than in the Ajd_{rf-f0} reference one. There is a decrease of these centers as aging increases from A20d to A110d in the Ajd_{fn} layers. This aging property is also valid in the aged reference Ajd_{rf-f0} layer although associated to a much stronger A110d reduction of the non-radiative recombination centers under illumination. The aging-induced recovery of the 1st PL intensity is severely damped by the introduction of the A0d_{fn-c_{ir}} irradiation defects. It is worth noting that this irradiation-induced quenching of the aging recovery of the Ajd_{fn} 1st PL intensity occurs without any correlation to the energy of the Ajd_{fn} emission transitions and FWHM associated to shallow levels in the Ajd_{fn} aged irradiated layers. It follows that the radiative shallow and non-radiative, a priori deep, electronic levels under illumination are associated to two different natures of under illumination-active defect population. Most likely, as in the Ajd_{rf-f0} reference and pristine rf-17 layer, chemical

reactions during the (3 min, 454 nm, air, ~ 300 K) illumination modify the initial A_{jd_fn} aging-induced defect population. The kinetics and/or nature of these chemical reactions evolve with the $A_{0d_fn-c_{ir}}$ irradiation defects.

Irradiation-induced aging and illumination defects under continuous illumination: PL versus illumination-time The effect of continuous illumination on the photoluminescence has distinctive features in the $GA_{0.015}Cs_{0.046}MA_{0.152}FA_{0.787}Pb(I_{0.815}Br_{0.185})_3$ layers depending on their quality: pristine (rf-17), aged after preparation (A_{jd_rf-f0}) or irradiated after 7d aging and, further, subsequently aged (A_{jd_fn}).

Continuous illumination in the pristine rf-17 layer (488 nm, 2548 W/cm², air, ~ 300 K). The PL peak energy and FWHM evolutions during the 5 h of illumination in rf-17 show that the PL spectra are formed of an evolving superposition of components with the contribution of the lower energy components increasing with illumination time. At the end of the 5 h illumination, the PL peak energy in the pristine rf-17 layer when compared to the bandgap, 1.64(1) eV, display a strong redshift with value in eV, rf-17-dE_{pg-300K}(300th)~0.058(1). This redshift is much higher than the initial Urbach energy in the pristine layer, ~0.018 eV. Its value is about those of the Urbach energy induced by aging in A_{jd_rf-f0} , 52–59(2) eV. This suggests that illumination under air generates defects in rf-17 that give rise to a distribution of shallow electronic levels.

In addition, illumination is associated in rf-17 to a strong photo-quenching of the PL intensity. One question is whether light produces two types of defects in rf-17, those at the origin of the broadening of the band tails and those responsible for the intensity photo-quenching. The small decrease of the energy and intensity between the 30th and 300th, –20% and –10%, respectively, shows that both distributions are mainly produced during the first 30 min of illumination.

Light illumination effects have been extensively investigated in HOIPs in the recent years. Results give evidence that different behaviors are reported depending on the illumination conditions (atmosphere, temperature) and on HOIPs composition and types (crystals, layer/substrates, encapsulated layer/substrates, active layers in solar cells, etc.) [34].

In $MAPbI_3$, for example, illumination at room temperature is reported to induce an increase of the PL peak intensity in layer/glass under N_2 and air atmosphere [10, 35] or in single crystals under air or argon atmosphere (Tian2015). The origin of this so-called light soaking effect is attributed to light-induced iodide migration [35] or to oxygen induced-curing of defects [11]. In the first case [35], using Time-of-flight secondary ion-mass spectroscopy (ToF-SIMS), the authors demonstrate that iodide ions migrate away from the laser spot during illumination. The PL peak energy remains constant

under illumination. The PL intensity at the laser spot can be reversibly restored in dark. The authors propose that a charge space induced by the laser illumination creates a local electrical field that drifts iodide ions away from the illuminated region. In the second case [11], the PL intensity increase is reported for illumination of crystals in air. The authors attribute the PL intensity enhancement with illumination-time to a photochemical reaction involving oxygen which passivates deep-lying trap defects.

In mixed halide HOIPs where the X site is occupied by a mixing of I- and Br- anions, illumination is reported to shift the PL peak energy to lower energies [12, 36–38]. This effect referred as the “Hoke effect” is observable for light intensities higher than 1 sun [34] and is reversible in dark when the light is switched off. The physical origin of this effect is under debate. Local heating induced by laser illumination is excluded [34, 38]. For some authors, light induces a halide segregation resulting in the formation of iodide-rich and bromide-rich domains which have different bandgaps [36, 37]. The lower ones are associated to Iodide rich domains that trap carriers. For others, it is a defect-assisted mechanism where halide ions migrate away from the light-excited HOIPs surface via halide defects [12, 38]. An investigation of the dependence of the “Hoke effect” with the Br/I stoichiometry of the solution used for the solution-process growth indicates that it is present for solution that have a Br content greater than 20% [3, 34]. The role of excess halide precursor during preparation has also been considered as playing a role [38]. The role of atmosphere has also been investigated in $MAPb(Br_{0.5}I_{0.5})_3$ /quartz and $PMMA/MAPb(Br_{0.5}I_{0.5})_3$ /quartz layers [12]. The repetition of illumination(15 s)/dark(30 min) cycles in vacuum, air and nitrogen atmosphere shows that the PL spectra are composed of different PL peaks with energy and intensity evolving with the number of cycles. The peaks in the range, 1.610/(770)–1.722/(720) (eV/(nm)), are attributed to iodide-rich phase. Those in the range, 1.878/(660)–1.937/(640) (eV/(nm)) are attributed to bromide-rich phase. For the lower energy peaks, there is an increase of the PL intensity with the number of illumination cycles independently on the atmosphere. The illumination-induced (15 s) variations reversibly evolves during the dark period (30 min). The reversible effect is stronger for illumination under inert nitrogen and PMMA covered layers.

In the present work, the PL peak energy decrease with increasing illumination time is observed in the $GA_{0.015}Cs_{0.046}MA_{0.152}FA_{0.787}Pb(I_{0.815}Br_{0.185})_3$ HOIP rf-17 layer obtained via a solution growth process from a solution with a nominal bromide content of 18.5%, and for an illumination intensity higher than 1sun. The light intensity corresponds to the conditions reported in literature [3, 34] for such a process to occur while the bromide content in the solution is slightly lower. It is worth noting that the PL spectra are single peak in the pristine rf-17 quadruple cation and double mixed halide (I,Br) HOIP and double peaks in the $MAPb(Br_{0.5}I_{0.5})_3$

single cation double mixed halide (I,Br) HOIP [12]. The energy with increasing illumination shifts in rf-17 from 1.6426(5) to 1.6041 (5) eV during the first 30 min of illumination and, further, to 1.5865(5) eV during the 300 min. This last energy is lower for ex. than any of those reported for the light-induced evolution in MAPb(Br_{0.5}I_{0.5})₃ [12]. One another striking property in rf-17 is the difference in the time scale evolution for the FWHM PL peak and those for the energy and intensity PL peak. The PL peak FWHM in rf-17 goes on evolving on long illumination timescale (300 min) whereas the PL peak energy and intensity in rf-17 tend to evolve towards quasi-stationary after much shorter time scale, 30 min instead of 300 min.

In summary, the pristine rf-17 GA_{0.015}CS_{0.046}MA_{0.152}FA_{0.787}Pb(I_{0.815}Br_{0.185})₃HOIP layer has an illumination time induced redshift of the PL peak spectra consistent with those previously reported for other mixed (I,Br) halide HOIPs with higher nominal Br content, $\geq \sim 20\%$ [3, 34]. The long and high power density illumination in rf-17 under air at 300 K has strong effects—a PL peak redshift (~ 58 meV) associated to a PL FWHM broadening (+ 100 meV) and PL intensity photoquenching (-96%). Whether under dark after such an illumination, the PL spectra in rf-17 recover their initial state remains an open question.

Continuous illumination in the Ajd_rf-f0 layer (454 nm, 1.1 W/cm², air, ~ 300 K) The light intensity in the aged reference Ajd_rf-f0 layer -1.1 W/cm² (11 sun)- is about three orders of magnitude less than in the pristine rf-17 layer -2548 W/cm² (25,480 sun). The peak decrease between 3 and 30 min is however of the same order in both layers -only about twice smaller in A20d_rf-f0 than in rf-17, 0.007 eV instead of ~ 0.015 eV. The photoquenching of the peak intensity also remains of the same order, approx. -60% instead of approx. -90% . The striking difference is that the 30 min illumination induces opposite FWHM variations of an order of magnitude less in A20d_rf-f0 than in rf-17, approx. -0.001 eV instead of ~ 0.010 eV.

With increasing duration, 20d(A20d-A0d), 53d(A53d-A0d), and 110d(A110d-A0d), the decrease of the PL(nth) peak energy and FWHM in the Ajd_rf-f0 layer remains monotonous with increasing illumination time. The photoquenching of the peak intensity is however strongly reduced with the peak intensity between 3 and 30 min illumination decreasing by approx. -60% for A20d to, only, approx. -10% for A53d and approx. -30% for A110d.

When illumination starts, the Ajd_rf-f0 aged reference layer differs from the pristine rf-17 one by the width of the aging-induced Ajd band tails. The associated Urbach energies are $\sim 53(2)$ meV (Table 3) in A20d_rf-f0 and $18(2)$ meV in rf-17. In addition, there is a sub-bandgap distribution of deep levels present in the Ajd-rf-f0 layer that is absent in rf-17. The 30 min illumination generates similar effects in the Ajd-rf-f0 and rf-17 as concern the evolution of the PL peak energy and

intensity. A red-shift of the emission transition is associated to its photoquenching under illumination. Furthermore, the PL peaks are composed of overlapping emission transitions that evolves in both cases under illumination. The photoquenching damping under illumination is independent on the initial Ajd_rf-f0/A20d_rf-f0 peak intensity ratio as aging increases. It is however minimum for the A53d aging where this ratio goes through a minimum. Plausible reason to these evolutions is that illumination generates defects. These illumination-induced defects give rise to near band edge distribution of shallow electronic states that act as radiative recombination centers with decreasing emission energy.

Continuous illumination in the Ajd_fn layers The A0d_fn-c_{irr} concentrations of irradiation defects have long term effects on the Ajd_fn (j(d) = 20, 53, 110) illumination-time dependence of the PL spectra that last over at least 110d.

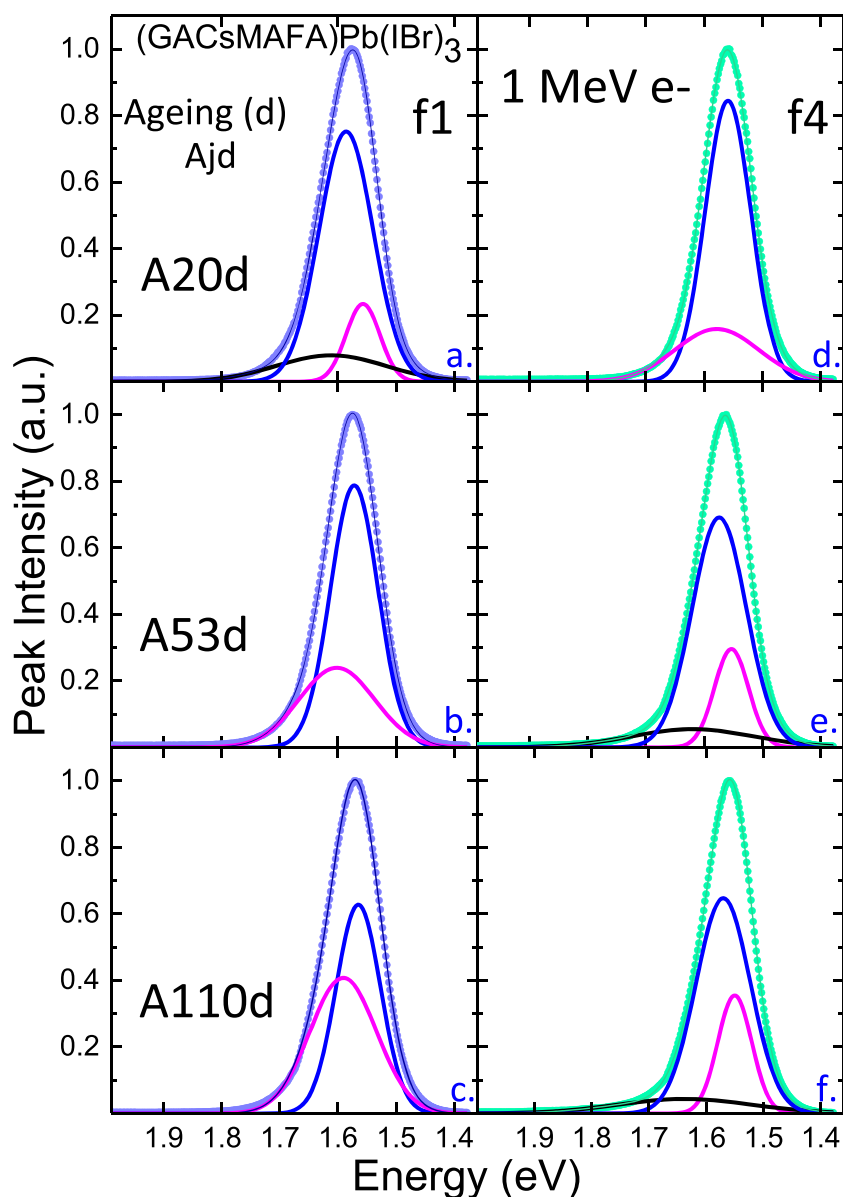
- (i) The PL spectra in the Ajd_fn aged irradiated layers have Ajd_fn illumination-time dependence that, after each Ajd aging, depends on the A0d_fn-c_{irr} initial concentrations.
- (ii) The concentrations affect also the correlations between the illumination-induced variations of the Ajd_fn peak energy, FWHM and intensity.
- (iii) The evolution of the correlations is reflected in the evolution of the Ajd_fn PL spectra deconvolution into several emission components.

The effects of the A0d_fn irradiation defects on the PL peak deconvolution are illustrated in Fig. 8 for the last Ajd_f1/f4 PL(6th) spectra recorded respectively for the f1 and f4 fluences at the end of the 30-min illumination after each Ajd aging. The deconvoluted Gaussian components—number, emission energy, FWHM, height—evolve as the A0d_fn-c_{irr} concentration of irradiation defects increases from the lower concentration, A0d_f1-c_{irr}, to the higher one, A0d_f4-c_{irr}.

With increasing duration, 20d(A20d-A0d), 53d(A53d-A0d), and 110d(A110d-A0d), the Ajd_f1-PL(6th) spectrum is deconvoluted into three emission components for the A20d_f1 PL(6th) peak (Fig. 8a) and two for the A53d/110d_f1 ones (Fig. 8b, c). For the Ajd_f4-PL(6th) spectrum, the deconvolution yields two components for the A20d_f4-PL(6th) peak (Fig. 8d) and three for the A53d/110d_f4-PL(6th) one (Fig. 8e, f). The main Gaussian components with a peak height, Ajd_fn-H_p > 0.6, have peak energies that decrease with increasing Ajd aging for f1 and go through a weak maximum for f4. The values in eV are respectively (Table 6):

$$\begin{aligned} & \text{A20d_f1-1.586; A53d_f1-1.572; A110d_f1-1.565.} \\ & \text{A20d_f4-1.559; A53d_f4-1.574; A110d_f4-1.570.} \end{aligned}$$

Fig. 8 Deconvolution in Gaussian emission components of the 6th PL spectra recorded after aging and 30 min of illumination in (GACsMAFA)Pb(IBr)₃ HOIPs for the 1 MeV e-irradiated Ajd_fn layers at the f1 and f4 fluences. The conditions for the Ajd aging are j(d) = 20/53/110 under N₂ atmosphere in dark at ~ 300 K. Two cycles of 15 min of illumination—light (15 min); dark (3 min); light (15 min)—are performed before the 6th spectra recording



To locate the ionization levels associated to the emission energy, the assumption is that the Ajd_fn bandgaps remain unchanged under 30 min 454 nm air illumination. The A20d_fn ionization levels contributing to the A20d_fn radiative recombinations are located within 44 meV from the conduction/valence band extrema in the A0d_f1 layer and 71 meV in the A0d_f4 one. It follows that the higher A0d_f4-c_{ir} irradiation defect concentration favors A20d_fn shallow electronic levels that are (-0.027) eV deeper in the bandgap for the A20_f4 layer than for the A20d_f1 one. With further increasing aging duration, the Ajd_fn ionization levels contributing to radiative recombinations remain located within ~44(3) meV from the conduction/valence band extrema in the A53d/A110d_f1 layer. They become much shallower, within ~26 and ~10 meV from the conduction/valence band extrema, in the A53d_f4 and A110d_f4 layer, respectively.

Effect of irradiation defects on decay lifetimes and their aging dependence After each Ajd aging (j(d) = 20, 53, 110), the Ajd_rf-f0/_fn TRPL spectra are recorded in the aged Ajd_rf-f0 reference and Ajd_fn irradiated layers after the 3 min in dark at the end of the continuous 30 min illumination at 454 nm in air. The TRPL energy windows are chosen with appropriate centers and widths to include the peak energy of the Ajd_rf-f0/_fn-PL(nth) spectra, 4 ≤ n ≤ 6. The Ajd_rf-f0/_fn TRPL spectra are recorded over spots that are within the larger Ajd_rf-f0/_fn PL spots where the Ajd_rf-f0/_fn-PL(1st-6th) spectra are recorded. One considers that the Ajd_rf-f0/_fn-TRPL spectra are recorded for layer states that are the same as during the recording of the Ajd_rf-f0/_fn-PL(6th) spectra. This is valid as far as the 3 min dark lets quasi-unperturbed the layer state obtained at the end of the recording of the Ajd_rf-f0/_fn-PL(6th) spectra. Given that this is the case for the first

Table 6 Deconvolution of the 6th photoluminescence spectra into Gaussian emission components after aging in (GACsMAFA)Pb(I₂Br)₃ HOIPs for the 1 MeV e-irradiated Ajd_{fn} layers at the f1 and f4 fluence.

Ajd _{fn} -Epi /FWHMi/ Hpi@Ep	Ep1 (eV)	FWHM1 (eV)	Hp@Ep1	Ep2 (eV)	FWHM2 (eV)	Hp@Ep2	Ep3 (eV)	FWHM3 (eV)	Hp@Ep3
A20d-f1	1.557	0.097	0.182	1.586	0.155	0.740	1.612	0.309	0.074
A53d-f1	1.572	0.136	0.784	1.602	0.216	0.220	–	–	–
A110d-f1	1.565	0.127	0.618	1.591	0.191	0.385	–	–	–
A20d-f4	1.559	0.131	0.844	1.578	0.240	0.152	–	–	–
A53d-f4	1.553	0.098	0.283	1.574	0.155	0.667	1.620	0.348	0.047
A110d-f4	1.550	0.099	0.343	1.570	0.158	0.626	1.637	0.390	0.035

The conditions for the Ajd aging are $j(d) = 0/53/110$ under N₂ atmosphere in dark at ~300 K. Epi, FWHM, Hpi@Epi are respectively the peak position, FWHM, and ratio height for the *i*th component

3 min dark period between the Ajd_{rf-f0}/_{fn}-PL(3rd) and Ajd_{rf-f0}/_{fn}-PL(4th) spectra, it is also most likely the case between the recording of the Ajd_{rf-f0}/_{fn}-PL(6th) and of that of the Ajd_{rf-f0}/_{fn}-TRPL spectra. The applied light power density has an average value much lower for the TRPL pulsed illumination than for the PL continuous illumination: 3×10^{-4} W/cm² ($\sim 3 \times 10^{-3}$ sun) instead of 1.1 W/cm² (~ 11 sun). It is valid to correlate the decay lifetime components resolved in the Ajd_{rf-f0}/_{fn}-TRPL spectra to the emission transitions deconvoluted in the Ajd_{rf-f0}/_{fn}-PL(6th) as far as the dominant populated ionization levels are the same under the TRPL and PL illumination conditions. It is assumed to be so hereafter although there is one order of magnitude difference between the respective light intensities. This is consequently to be considered as a tentative correlation for the determination of which emission transitions are associated to the longer decay lifetimes in the aged Ajd_{rf-f0} reference and Ajd_{fn} irradiated layers.

The average lifetimes associated to the Ajd_{rf-f0}/_{fn}-TRPL spectra have values in μ s, Ajd_{rf-f0}/_{fn}- $\langle\tau_{Pn}\rangle_{Pn}$: 2.0–4.5. This reflects the exceptionally long lifetimes associated to the longer lifetime decay component resolved in the Ajd_{rf-f0}/_{fn}-TRPL spectra. The lifetime and intensity associated to this longer component vary over ranges in (μ s; %), Ajd_{rf-f0}/_{fn}- $[\langle\tau_2\rangle_{Pn}; \langle I_2\rangle_{Pn}]$ - $[\sim(2.8-6.9); (26-49)]$. The shorter Ajd_{rf-f0}/_{fn}- $\langle\tau_1\rangle_{Pn}$ lifetimes vary over a much lower range, $\sim 0.74-2.0$ μ s, with intensity always higher than $\sim 50\%$.

It is interesting to notice that, after the 30 min illumination in the Ajd_{fn} aged irradiated layers irradiation-induced aging defect populations, the average lifetime, the short and long lifetimes vary non-monotonously with the A0d_{fn-c_{ir}} irradiation defect concentrations initially introduced in the fn irradiated layers. The most puzzling is that the higher A0d_{f4-c_{ir}} irradiation induces a steep increase for the three of them and for the I₂ intensity of the longer lifetime component. They all then reach their maximum values, respectively in ns, A20d_{f4}- $[\langle\tau_{Pn}\rangle_{Pn}, \langle\tau_1\rangle_{Pn}, \langle\tau_2\rangle_{Pn}] \sim [4500, 2000, 6900]$ and in %, A20d_{f4}- $\langle I_2\rangle_{Pn} \sim 50$. This is no longer the case

for the A53d and A110d aging where the A0d_{fn-c_{ir}} dependence of the lifetimes and intensity have different characteristics. The complex aging behavior of the Ajd_{fn}- $\langle\tau_{Pn}\rangle_{Pn}$ - $\langle\tau_1\rangle_{Pn}$ - $\langle\tau_2\rangle_{Pn}$ - $\langle I_1\rangle_{Pn}$ - $(1-\langle I_1\rangle_{Pn})$ lifetimes and intensities confirms that illumination-induced processes after each aging are dependent on the A0d_{fn-c_{ir}} concentration of irradiation defects initially introduced in the layers. The nature of the ionization levels involved in the radiative recombination under the 482 nm pulsed illumination seem to evolve the less for the higher A0d_{fn-c_{ir}} concentration of irradiation defects $f2 \leq fn \leq f4$ after the A53d and A110d aging.

For the A20d aging, it is possible to examine the correlation as a function of increasing A0d_{fn-c_{ir}} irradiation defects between the evolution of (i) the deconvolution of the PL spectra into Gaussian emission transitions and (ii) the resolution of the TRPL into exponential lifetime components. This correlation shows that the energy decrease, ~ 0.025 eV, from A20d_{f1}-1.586 to A20d_{f4}-1.559 eV (Table 5) corresponds to the—seen above—strong increase of the lifetimes and intensity of the longer lifetime. It follows that the main transition in the A20d_{f4} layer is characterized by the energy and the decay lifetime, A20d_{f4}- $[Ep, \langle\tau_2\rangle_{Pn}]$ (eV, ns)- $(\sim 1.559; \sim 6900)$.

The correlation between (i) and (ii) as a function of increasing aging duration yields to the determination of the characteristics—peak energy and decay lifetime—of the Ajd_{f1/f4} emission transitions in the aged Ajd_{f1} and Ajd_{f4} irradiated layers. As aging duration increases by 47d(A53d-A110d), for both A0d_{f1-c_{ir}} and A0d_{f4-c_{ir}} concentrations, the energy of the main emission remains quasi the same whereas the average decay lifetime $\langle\tau_{Pn}\rangle_{Pn}$ increases by 63% for A0d_{f1-c_{ir}} and 9% for A0d_{f4-c_{ir}}. The respective characteristics of the A53d/A110d_{f1} emission transitions associated to the longer lifetimes are A53/A110d_{f1}- $[Ep; \langle\tau_2\rangle_{Pn}]$ (eV, ns)- $\sim [1.568(1)''; \sim 4121(102)/5279(404)]$. Those for the A53d/A110d_{f4} ones are A53/A110d_{f4}- $[Ep; \langle\tau_2\rangle_{Pn}]$ (eV, ns)- $\sim [1.562(1)''; \sim 4983(496)/5695(164)]$.

The photocarrier recombination dynamics in absence of local electrical fields after a laser pulse depend on the initial

density of photoionized carriers $n(0)$ and on the radiative and non-radiative available recombination channels [39, 40]. The charge carrier dynamics is generally considered to be dominated by trapping at non-radiative recombination centers in HOIPs for photoionization regime where $n(0)$ is much smaller than these center concentration, N_{nr} [41–43]. According to various reports, the N_{nr} density in pristine MAPI thin films is reported to be around $10^{16-17} \text{ cm}^{-3}$ [41] and around 10^{15} cm^{-3} for other mixed halide perovskites [44]. For the photoexcitation conditions in this work, given the laser energy per pulse applied, spot and wavelength, the density is expected to be $\sim 10^{13} \text{ cm}^{-3}$ for the initial photoionized carrier density. It is consequently lower than the density for the non-radiative centers previously reported in pristine HOIPs and those expected in the aged A_{jd_fn} irradiated layers.

The predominant decay lifetime in the A_{20d_rf-f0} aged reference layer, 4.2 μs , is longer than those previously reported, $\sim 3.1 \mu\text{s}$, in $\text{GA}_{0.25}\text{MA}_{0.75}\text{PbI}_3$ pristine layer on glass [45]. This may reflect the difference in the illumination conditions before the measurements of the decay lifetimes. In the present work, there is 30 min of 454 nm continuous illumination in air at $\sim 300 \text{ K}$ before the TRPL measurements. It might also reflect the difference in aging after preparation. One notices indeed that there is a systematic increase of the shorter and longer carrier lifetimes in A_{jd_rf-f0} as aging increases from 27d(A_{20d}) to 117d(A_{110d}) after their preparation: $A_{jd_}[\langle\tau_1\rangle_{p_n}, \langle\tau_2\rangle_{p_n} (\mu\text{s})]$: $A_{20d_} \sim [1.2, 4.2]$; $A_{110d_} \sim [1.9, 6.8]$. It is also associated to an increase of the fraction of ionized carriers that recombine with the longer lifetime.

It has been earlier reported in MAPbI_3 layer on glass [42] that the single component decay lifetime recorded at room $T(\text{K})$ as a function of pulsed excitation intensity is longer for 48 h Ar aged states than for fresh ones. Above a threshold of excitation intensity where bimolecular carrier recombination starts to occur for both states, it is no longer the case. Furthermore, for fresh states at a given pulsed excitation intensity corresponding to the monomolecular recombination regime, the radiative decay lifetimes increase as time elapses. This feature is associated to constant PL spectra. It is referred as self-annealing at room temperature, and is attributed by the authors to a decrease of shallow non-radiative defects and unintentional dopants.

In $\text{GA}_x\text{MA}_{1-x}\text{PbI}_3$, the GA cations appear to play a key role for the existence of long lifetimes $\sim 3.2 \mu\text{s}$ [45]. TRPL measurements were performed in air and room temperature for polycrystalline HOIPs on glass substrates including a mix of MA and GA cations, $\text{GA}_x\text{MA}_{1-x}\text{PbI}_3$ with x increasing in the range [0, 0.05, 0.1, 0.25]. The long lifetime in the (multicomponent) lifetime spectra associated to the x values varies in the range $-0.080, 0.9, 3.1, 0.3 \mu\text{s}$ - and goes through a maximum of 3.1 μs for $x = 0.1$. The authors

attribute the two orders of magnitude higher lifetime upon GA incorporation at $x = 0.1$ to a faster capability of reorientation for GA than MA in $\text{GA}_x\text{MA}_{1-x}\text{PbI}_3$. From DFT calculations, it was reported that quicker rotations of the organic cations result in longer lifetimes of the carriers ionized in the conduction/valence band [46]. The cation rotations enable the formation of shallow traps with the ionized carriers, which extends the carrier lifetime.

In summary, the coupling of electron irradiation with subsequent aging exhibits a striking effect on the carrier radiative lifetime at the end of illumination (30 min, 454 nm, 1.1 Wcm^{-2} , air, 300 K) after 20 days of aging. The higher A_{0d_f4-cir} irradiation defect concentration promotes a carrier lifetime about 2.46 longer than in $rf-f0$ with a value reaching $\sim 6.9 \mu\text{s}$. This lifetime increase is associated to a low emission transition, 1.559 eV, and a photoquenching of $\sim 20\%$ with respect to the PL intensity in A_{0d_rf-f0} .

Aging and electron irradiation defects: nature This paragraph discusses the possible nature of the defects that can be generated during the various treatments investigated here (N_2 atmosphere, dark, $\sim 300 \text{ K}$) aging, 1 MeV electron irradiation, continuous illumination. It also discusses some properties of their interaction that can be derived from their effects on optical properties.

Clearly, the $\text{GA}_{0.015}\text{Cs}_{0.046}\text{MA}_{0.152}\text{FA}_{0.787}\text{Pb}(\text{I}_{0.815}\text{Br}_{0.185})_3$ layers have the usual properties reported in ABX_3 compounds where only one type of cations or halide occupies the A and X sites [2]. They are prepared in thermodynamically metastable states that slowly evolve towards quasi-equilibrium states that are dependent on the environmental conditions. One-megaelectronvolt electron is used in this work to control intrinsic defects in HOIPs. Little is known in literature about the damage that 1-MeV electron beam produced in HOIPs. There are more reports on the damage observed in vacuum under the beams used for scanning electron microscopy (SEM) at much (5–10 keV) lower energy and higher flux [47] and for transmission electron microscopy (TEM) [48, 49]. On the contrary, the conditions for the 1-MeV irradiation are chosen in this work to preserve the integrity of the layers and prevent their decomposition under irradiation.

The APbX_3 crystalline and chemical structure of the set-18 layers has interesting properties as concern the slowing-down of the 1-MeV electron beam. As well documented since decades (for example, see references in [50–52]), the energy transfer from the beam electrons to the target occurs via elastic collisions with target nuclei, and, via inelastic collisions with target electrons. The elastic collisions generate vacancy-interstitials pairs via replacement collision sequences along the crystalline directions with lower threshold energy displacements [53]. The inelastic ones generate electronic excitation or secondary electrons via ionization. In the $\text{GA}_{0.015}\text{Cs}_{0.046}\text{MA}_{0.152}\text{FA}_{0.787}\text{Pb}(\text{I}_{0.815}\text{Br}_{0.185})_3$ set-18 layers, the Pb and X(I,Br) sublattices occupied by inorganic elements are sensitive to the nuclear stopping power. The damage on the respective sublattices is the production of Pb or X type

vacancy - interstitial Frenkel pairs with distributed separation distances. The halide sublattice is occupied by a disordered (I, Br) halide solid solution with a nominal content of 18.5% for the halide sites occupied with Br_x . The probability that a replacement collision sequence ends up in a Frenkel pair production decreases with increasing nuclei mass. Consequently, 1 MeV e-irradiation likely produces higher concentrations of halide Frenkel pairs than lead ones in the set-18 layers. Br being lighter than iodine, the probability of the formation of Br interstitial-halide vacancy is high. The halide interstitial distribution is expected to be richer in interstitial of the Br_i type than the nominal percentage of Br_x located on the halide sites. The A sublattice, mostly occupied by organic molecular cations (MA, FA, GA), is mainly sensitive to the electron stopping power that excites or ionizes them [51]. Both their excitation and ionization are expected to be fast dissipated by interaction with the ionized carriers in the APbX_3 valence and conduction band. Calculations are beyond the scope of this work to check that indeed the number of displaced A cations or of their elements (for example, H) is rather low.

At A0d, in the set-18 layers 7d aged after preparation, 1 MeV e-irradiation progressively removes the initial sub-bandgap distribution of deep electronic levels and replaces them with irradiation-induced ones. Depending on the Fermi level position and cation/halide stoichiometry, the defects associated to deep levels in MAPbI_3 , MAPbBr_3 and FAPbI_3 [54–56] are the deep donor I_{pb} , I_{MA} , Pb_{Br} antisites, the deep acceptor I_{FA} , Pb_i antisites and the deep acceptor Pb_i interstitials. The ionization levels are located between 0.2–0.5 eV from the valence band maximum or conduction band minimum. The replacement collision sequences along the halide sublattice direction of minimal threshold displacement have the cleaning effect of removing the deep levels associated to the A cation (MA, FA, GA) occupying antisite location in the halide sublattice, I_A . The replacement collision sequences along the Pb sublattice directions of minimal threshold displacement can remove the deep levels associated to the halide (I,Br) elements, X_{pb} , occupying an antisite location in the Pb sublattice. They can also introduce deep levels associated to Pb_i interstitials when succeeding in producing Pb vacancy-interstitial Frenkel pairs.

The width of the band tails with increasing A0d_{fn-c_{ir}} irradiation concentration evolves with a non-monotonous concentration dependence. On the basis of the shallow levels expected in MAPbI_3 , MAPbBr_3 and FAPbI_3 [54–56], this may reflect the introduction of shallow donor A_i (MA,FA,GA) interstitials by removal of A_x antisites, of shallow donor V_x (X: I,Br) vacancies and shallow acceptor X_i (X:I,Br) interstitial by the production of halide vacancy-interstitials pairs as well as the introduction of shallow acceptor V_{pb} vacancies by the production of lead vacancy-interstitials pairs. One question is whether the presence of the guanidinium organic cations, $(\text{C}(\text{NH}_2)^+)_3$, can stabilize halide vacancies. Their quicker

rotations may enable to locate one hydrogen of the H-N bonding in the vicinity of a vacancy. Furthermore, the resonance of the positive charge in this moiety may enable to locate it away from the halide vacancy when this vacancy is positively charged. Another one is whether the Ajd_{fn} band tails result in donor or acceptor doping with higher n-type or p-type conduction in the Ajd_{fn} irradiated layers than in the $\text{Ajd}_{\text{rf-f0}}$ layer or, rather, to donor-acceptor compensation.

The irradiation-induced aging behavior tends to shrink the bandgap with a non-monotonous concentration dependence. The Ajd_{f1} irradiated layer has bandgap values close to those of the $\text{Ajd}_{\text{rf-f0}}$ reference layer. The bandgaps are lower in the Ajd_{fn} ($f_2 \leq f_n \leq f_4$) irradiated layers with fluences in the range [f_2 - f_4] than in the aged $\text{Ajd}_{\text{rf-f0}}$ reference one. On the basis that MAPbI_3 has a lower bandgap than MAPbBr_3 (for ex. [36]), this points out to an irradiation-aging assisted iodine enrichment of the halide distribution on the halide sublattice. One plausible reason is that migrating iodine interstitials, I_i , preferentially fill the halide vacancies, V_x , or exchange positions with bromide occupied halide sites, Br_x . This exchange results in iodine relocation on halide sites, I_x and replaces I_i interstitials with Br_i interstitials. It consequently enriches the interstitial populations with Br_i .

Some authors suggest that a unique feature of HOIPs is that any dangling bond-like defect or associated defect complexes will have transition states close to the band edges [57]. If this statement is correct, this suggests that the irradiation-aging assisted broadening of the band tails arise from the formation of dangling bond-like defect or associated defect complexes. This may reflect that the irradiation-aging assisted Br depletion of the halide distribution on the halide sublattice sites results in halide vacant sites, i.e., V_x .

Under 454/488 nm illumination in air, the set-18 layers evolve towards states that result from the surface reactivity with oxygen, nitrogen, water vapor that are not photolyzed at these wavelengths. The reactions at the surface of the pristine rf-17 and 7d aged rf-f0 references layers are expected to differ given the different wavelength and power density used for the continuous illumination in air. The comparison between the layer evolutions under continuous illumination can be misleading as concern the origin of the differences. This is why it is no further discussed here.

5 Conclusion

This work reports the first experimental data on the effects of intrinsic defects on the aging properties of the emergent $\text{GA}_{0.015}\text{Cs}_{0.046}\text{MA}_{0.152}\text{FA}_{0.787}\text{Pb}(\text{I}_{0.815}\text{Br}_{0.185})_3$ HOIPs. For this purpose, the optical properties of $\text{GA}_{0.015}\text{Cs}_{0.046}\text{MA}_{0.152}\text{FA}_{0.787}\text{Pb}(\text{I}_{0.815}\text{Br}_{0.185})_3$ layers prepared on glass were investigated as a function of aging duration after gradually increasing concentrations of intrinsic

defects were produced in the HOIP layers through high-energy electron irradiation (1 MeV). Optical absorption, photoluminescence under continuous laser illumination and time resolved photoluminescence performed before and after increasing aging periods (N_2 , dark, ~ 300 K) up to 110 days confirmed the stabilization effects of intrinsic defects in quadruple HOIPs.

The existence of similar effects remains to be confirmed in $MAPbI_3$ for which solar cells are reported to exhibit radiation resistance to 1 MeV electron irradiation [6, 7] or 50 keV or 68 MeV protons [6–8] and in other HOIPs compounds to confirm their ability to sustain space environment as active layers in photovoltaic devices.

The comparison of the absorption properties in aged and pristine $GA_{0.015}Cs_{0.046}MA_{0.152}FA_{0.787}Pb(I_{0.815}Br_{0.185})_3$ layers showed that naturally aging (7d, N_2 , dark, ~ 300 K) produced two types of aging-induced defect populations affecting the width of the energy distribution of shallow traps that becomes broader than in pristine layers and distribution of deep traps acting as strong absorption centers. The fluences (fn) chosen in this work for the 1 MeV electron irradiation introduce intrinsic defects in 7d-aged $GA_{0.015}Cs_{0.046}MA_{0.152}FA_{0.787}Pb(I_{0.815}Br_{0.185})_3$ layers in a concentration range that leaves the bandgap in the layers unchanged. With increasing concentration of defects, the absorption and width variations were found to go through maxima indicating that various processes take place during irradiation and subsequent short A0d aging (< 1 day) periods.

In summary, the interplay of high-energy irradiation offers a new platform to engineer intrinsic defects in perovskite materials that in turn impart higher stability and improvement in functional properties. In addition, the change in fundamental properties such as bandgap shrinkage triggered by irradiation and enhanced optical absorption via deep subgap electronic level can provide innovative processing pathways to enhance the photovoltaics characteristics of HOIP devices.

Acknowledgements Authors are grateful to the University of Cologne, Cologne, Germany and Ecole Polytechnique, Palaiseau, France for the financial and infrastructural support. SM and EJ are grateful for the financial support from German Science Foundation (DFG) provided in the framework of the priority program “SPP 2196 - Perovskite semiconductors: From fundamental properties to devices”. PA is grateful to the Doctoral School of the Institut Polytechnique de Paris (ED IP Paris) for the financial support.

Funding Information Open Access funding provided by Projekt DEAL.

Compliance with ethical standards

Conflict of interest The authors declare that they have no conflict of interest.

Open Access This article is licensed under a Creative Commons Attribution 4.0 International License, which permits use, sharing, adaptation, distribution and reproduction in any medium or format, as long as you give appropriate credit to the original author(s) and the source,

provide a link to the Creative Commons licence, and indicate if changes were made. The images or other third party material in this article are included in the article's Creative Commons licence, unless indicated otherwise in a credit line to the material. If material is not included in the article's Creative Commons licence and your intended use is not permitted by statutory regulation or exceeds the permitted use, you will need to obtain permission directly from the copyright holder. To view a copy of this licence, visit <http://creativecommons.org/licenses/by/4.0/>.

References

1. NREL Best Research-Cell Efficiencies, <https://www.nrel.gov/pv/cellefficiency.html>
2. D.A. Egger, A. Bera, D. Cahen, G. Hodes, T. Kirchartz, L. Kronik, R. Lovrincic, A.M. Rappe, D.R. Reichman, O. Yaffe, What remains unexplained about the properties of halide perovskites? *Adv. Mater.* **30**, 1800691 (2018)
3. C.C. Boyd, R. Checharoen, T. Leijtens, M.D. McGehee, *Chem. Rev.* **119**(5), 3418–3451 (2019)
4. S. Wu, Z. Li, J. Zhang, T. Liu, Z. Zhu, A. Jen, Efficient large guanidinium mixed perovskite solar cells with enhanced photovoltage and low energy losses. *Chem. Commun.* **55**, 4315–4318 (2019). <https://doi.org/10.1039/C9CC00016J>
5. W. Zhang, J. Xiong, J. Li, W.A. Daoud, J. Mater. Chem. A (2019). <https://doi.org/10.1039/C9TA01893J>
6. Y. Miyazawa, M. Ikegami, H.-W. Chen, T. Ohshima, M. Imaizumi, K. Hirose, T. Miyasaka, *iScience* **2**, 148–155 (2018)
7. Y. Miyazawa, M. Ikegami, T. Miyasaka, T. Ohshima, M. Imaizumi, K. Hirose, *IEEE* (2015), <https://doi.org/10.1109/PVSC.2015.7355859>
8. F. Lang, N.H. Nickel, J. Bundesmann, S. Seidel, A. Denker, S. Albrecht, V.V. Brus, J. Rappich, B. Rech, G. Landi, H.C. Neitzert, Radiation hardness and self-healing of perovskite solar cells. *Adv. Mater.* **28**, 8726–8731 (2016)
9. O. Plantevin, S. Valère, D. Guerfa, F. Lédée, G. Trippé-Allard, D. Garrot, E. Deleporte, *Phys. Status Solidi B*, 1900199 (2019)
10. D.W. de Quilettes, S.M. Vorpahl, S.D. Stranks, H. Nagaoka, G.E. Eperon, M.E. Ziffer, H.J. Snaith, D.S. Ginger, *Science* **348**(6235), 683–686 (2015)
11. Y. Tian, A. Merdasa, E. Unger, M. Abdellah, K. Zheng, S. McKibbin, A. Mikkelsen, T. Pullerits, A. Yartsev, V. Sundström, I.G. Scheblykin, *J. Phys. Chem. Lett.* **6**(20), 4171–4177 (2015)
12. A.J. Knight, A.D. Wright, J.B. Patel, D.P. McMeekin, H.J. Snaith, M.B. Johnston, L.M. Herz, *ACS Energy Lett.*, **4**, 75–84 (2019, 2018)
13. J.A. Guerra, A. Tejada, L. Korte, L. Kegelmann, J.A. Töfflinger, S. Albrecht, B. Rech, R. Weingärtner, Determination of the complex refractive index and optical bandgap of $CH_3NH_3PbI_3$ thin films. *J. Appl. Phys.* **121**, 173104 (2017)
14. P. Nandakumar, C. Vijayan, Y.V.G.S. Murti, Optical absorption and photoluminescence studies on CdS quantum dots in Nafion. *J. Appl. Phys.* **91**, 1509–1514 (2002)
15. Ikhmayies2013, S.J. Ikhmayies, R.N. Ahmad-Bitar, *J. Mater. Res. Technol.* **2**(3), 221–227 (2013)
16. B.U. Haq, S. AlFaify, A. Laref, R. Ahmed, F.K. Buttd, A.R. Chaudhry, S.U. Rehmanf, Q. Mahmood, *Ceram. Int.* **45**, 18073–18078 (2019)
17. S. De Wolf, J. Holovsky, S.-J. Moon, P. Löper, B. Niesen, M. Ledinsky, F.-J. Haug, J.-H. Yum, C. Ballif, *J. Phys. Chem. Lett.* **5**, 1035–1039 (2014)
18. W. Rehman, D.P. McMeekin, J.B. Patel, R.L. Milot, M.B. Johnston, H.J. Snaith, L.M. Herz, Photovoltaic mixed-cation lead mixed-

- halide perovskites: links between crystallinity, photo-stability and electronic properties. *Energy Environ. Sci.* **10**, 361–369 (2017)
19. W. Li, K. Zhao, H. Zhou, W. Yu, J. Zhu, Z. Hu, J. Chu, Precursor solution temperature dependence of the optical constants, band gap and Urbach tail in organic–inorganic hybrid halide perovskite films. *J. Phys. D: Appl. Phys.* **52**, 045103 (2019)
 20. I. Studenyak, M. Kranjec, M. Kurik, *Int. J. Optics Appl.* **4**(3), 76–83 (2014)
 21. C. Kim, T.D. Huan, S. Krishnan, R. Ramprasad, A hybrid organic-inorganic perovskite dataset. *Scientific Data* **4**, 170057 (2017)
 22. A.K. Jena, A. Kulkarni, T. Miyasaka, *Chem. Rev.* **119**(5), 3036–3103 (2019)
 23. M. Samiee, S. Konduri, B. Ganapathy, R. Kottokkaran, H.A. Abbas, A. Kitahara, P. Joshi, L. Zhang, M. Noack, V. Dalal, Defect density and dielectric constant in perovskite solar cells. *Appl. Phys. Lett.* **105**, 153502 (2014)
 24. A.D. Wright, R.L. Milot, G.E. Eperon, H.J. Snaith, M.B. Johnston, L.M. Herz, Band-Tail Recombination in Hybrid Lead Iodide Perovskite. *Adv. Funct. Mater.* **27**, 1700860 (2017)
 25. F. Staub, H. Hempel, J.-C. Hebig, J. Mock, U.W. Paetzold, U. Rau, T. Unold, T. Kirchartz, Beyond Bulk Lifetimes: Insights into Lead Halide Perovskite Films from Time-Resolved Photoluminescence. *Phys. Rev. Appl.* **6**, 044017 (2016)
 26. P.M. Amirtharaj, *D. G. Seiler in Handbook of Optics, 2nd edn. Vol II, ed. By M. Bass* (McGraw-Hill, Inc., New York, 1995), p. 36.8
 27. G.M. Martin, Optical assessment of the main electron trap in bulk semi-insulating GaAs. *Appl. Phys. Lett.* **39**, 747–748 (1981)
 28. U. Zammit, K.N. Madhusoodanan, M. Marinelli, F. Scudieri, R. Pizzoferrato, F. Mercuri, E. Wendler, W. Wesch, Optical-absorption studies of ion-implantation damage in Si on sapphire. *Phys. Rev. B* **49**, 14322–14330 (1994)
 29. D. Ritter, K. Weiser, Suppression of interference fringes in absorption measurements on thin films. *Opt. Commun.* **57**, 336–338 (1986)
 30. A. Larena, F. Millan, G. Pérez, G. Pinto, Effect of surface roughness on the optical properties of multilayer polymer films. *Appl. Surf. Sci.* **187**, 339–346 (2002)
 31. J.K. Katahara, H.W. Hillhouse, Quasi-Fermi level splitting and sub-bandgap absorptivity from semiconductor photoluminescence. *J. Appl. Phys.* **116**, 173504 (2014)
 32. A.D. Wright, C. Verdi, R.L. Milot, G.E. Eperon, M.A. Pérez-Osorio, H.J. Snaith, F. Giustino, M.B. Johnston, L.M. Herz, Electron–phonon coupling in hybrid lead halide perovskites. *Nat. Commun.* **7**, 11755 (2016)
 33. L. Malikova, W. Krystek, F.H. Pollak, N. Dai, A. Cavus, M.C. Tamargo, Temperature dependence of the direct gaps of ZnSe and Zn_{0.56}Cd_{0.44}Se. *Phys. Rev. B* **54**, 1819–1824 (1996)
 34. D.J. Slotcavage, H.I. Karunadasa, M.D. McGehee, Light-Induced Phase Segregation in Halide-Perovskite Absorbers. *ACS Energy Lett.* **1**, 1199–1205 (2016)
 35. D.W. de Quilettes, W. Zhang, V.M. Burlakov, D.J. Graham, T. Leijtens, A. Osherov, V. Bulovic, H.J. Snaith, D.S. Ginger, S.D. Stranks, *Nat. Commun.* **7**, 11683 (2016)
 36. E.T. Hoke, D.J. Slotcavage, E.R. Dohner, A.R. Bowring, H.I. Karunadasa, M.D. McGehee, Reversible photo-induced trap formation in mixed-halide hybrid perovskites for photovoltaics. *Chem. Sci.* **6**, 613–617 (2015)
 37. S.J. Yoon, M. Kuno, P.V. Kamat, Shift happens. How halide ion defects influence photoinduced segregation in mixed halide perovskites. *ACS Energy Lett.* **2**, 1507–1514 (2017)
 38. A.J. Barker, A. Sadhanala, F. Deschler, M. Gandini, S.P. Senanayak, P.M. Pearce, E. Mosconi, A.J. Pearson, Y. Wu, A.R.S. Kandada, T. Leijtens, F. De Angelis, S.E. Dutton, A. Petrozza, R.H. Friend, Defect-assisted photoinduced halide segregation in mixed-halide perovskite thin films. *ACS Energy Lett.* **2**, 1416–1424 (2017)
 39. J. I. Pankove, *Optical processes in Semiconductors*, 1st edn. (Prentice-Hall, Inc., Englewood Cliffs, N-J, 1971), pp. 107–156
 40. J.R. Lakowicz, *Principles of fluorescence spectroscopy*, 3rd edn. (Springer, New York, 2006), p. 99
 41. L.M. Herz, Charge-carrier dynamics in organic-inorganic metal halide perovskites. *Annu. Rev. Phys. Chem.* **67**, 65–89 (2016)
 42. Y. Yamada, M. Endo, A. Wakamiya, Y. Kanemitsu, *J. Phys. Chem. Lett.* **6**, 482–486 (2015)
 43. S.D. Stranks, V.M. Burlakov, T. Leijtens, J.M. Ball, A. Gorieli, H.J. Snaith, Recombination Kinetics in Organic-Inorganic Perovskites: Excitons, Free Charge, and Subgap States. *Phys. Rev. Applied* **2**, 034007 (2014)
 44. A. Bercegol, F.J. Ramos, A. Rebai, T. Guillemot, D. Ory, J. Rousset, L. Lombez, *J. Phys. Chem. C* **122**(43), 24570–24577 (2018)
 45. D.J. Kubicki, D. Prochowicz, A. Hofstetter, M. Saski, P. Yadav, D. Bi, N. Pellet, J. Lewiński, S.M. Zakeeruddin, M. Grätzel, L. Emsley, *J. Am. Chem. Soc.* **140**(9), 3345–3351 (2018)
 46. J. Gong, M. Yang, X. Ma, R.D. Schaller, G. Liu, L. Kong, Y. Yang, M.C. Beard, M. Lesslie, Y. Dai, B. Huang, K. Zhu, T. Xu, *J. Phys. Chem. Lett.* **7**(15), 2879–2887 (2016)
 47. C. Xiao, Z. Li, H. Guthrey, J. Moseley, Y. Yang, S. Wozny, H. Moutinho, B. To, J.J. Berry, B. Gorman, Y. Yan, K. Zhu, M. Al-Jassim, *J. Phys. Chem. C* **119**(48), 26904–26911 (2015)
 48. B. Yang, O. Dyck, W. Ming, M.-H. Du, S. Das, C.M. Rouleau, G. Duscher, D.B. Geohegan, K. Xiao, *ACS Appl. Mater. Interfaces* **8**(47), 32333–32340 (2016)
 49. S. Chen, X. Zhang, J. Zhao, Y. Zhang, G. Kong, Q. Li, N. Li, Y. Yu, N. Xu, J. Zhang, K. Liu, Q. Zhao, J. Cao, J. Feng, X. Li, J. Qi, D. Yu, J. Li, P. Gao, Atomic scale insights into structure instability and decomposition pathway of methylammonium lead iodide perovskite. *Nat. Commun.* **9**, 4807 (2018)
 50. K. Nordlund, S.J. Zinkle, A.E. Sand, F. Granberg, R.S. Averback, R. Stoller, T. Suzudo, L. Malerba, F. Banhart, W.J. Weber, F. Willaime, S.L. Dudarev, D. Simeone, Improving atomic displacement and replacement calculations with physically realistic damage models. *Nat. Commun.* **9**, 1084 (2018)
 51. C.N. Shingledecker, R. Le Gal, E. Herbsta, A new model of the chemistry of ionizing radiation in solids: CIRIS. *Phys. Chem. Chem. Phys.* **19**, 11043–11056 (2017)
 52. N. Bohr, *Phil. Mag. S. 6*, 26: 151, 1–25 (1913)
 53. A.Y. Konobeyev, U. Fischer, Y.A. Korovin, S.P. Simakov, Evaluation of effective threshold displacement energies and other data required for the calculation of advanced atomic displacement cross-sections. *Nucl. Energy Technol.* **3**, 169–175 (2017)
 54. W.-J. Yin, T. Shi, Y. Yan, Unusual defect physics in CH₃NH₃PbI₃ perovskite solar cell absorber. *Appl. Phys. Lett.* **104**, 063903 (2014)
 55. A. Mannodi-Kanakkithodi, J.-S. Park, D.H. Cao, N. Jeon, A.B.F. Martinson, M.K.Y. Chan, *IEEE* (2015). <https://doi.org/10.1109/PVSC.2018.8547974>
 56. N. Liu, C.Y. Yam, First-principles study of intrinsic defects in formamidinium lead triiodide perovskite solar cell absorbers. *Phys. Chem. Chem. Phys.* **20**, 6800–6804 (2018)
 57. W. Walukiewicz, I. Rey-Stolle, G. Han, M. Jaquez, D. Broberg, W. Xie, M. Sherburne, N. Mathews, M. Asta, *J. Phys. Chem. Lett.* **9**(14), 3878–3885 (2018)